

U-Know-DiffPAN: An Uncertainty-aware Knowledge Distillation Diffusion Framework with Details Enhancement for PAN-Sharpening

Sungpyo Kim
KAIST

ksp04204@kaist.ac.kr

Jeonghyeok Do
KAIST

ehwjdgur0913@kaist.ac.kr

Jaehyup Lee[†]
KNU

jaehyuplee@knu.ac.kr

Munchurl Kim[†]
KAIST

mkimee@kaist.ac.kr

<https://kaist-viclab.github.io/U-Know-DiffPAN-site>

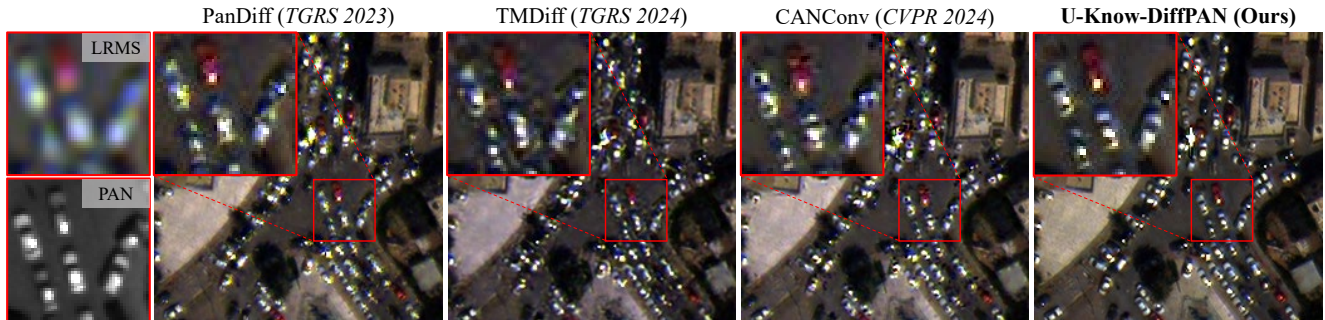


Figure 1. Visual comparison of PAN-sharpening results on the full-resolution WV3 dataset. The rightmost image shows the output of our proposed U-Know-DiffPAN framework, specifically the result produced by FSA-S (frequency selective attention student network). Notably, the proposed framework generates more detailed and robust results, particularly in high-uncertainty regions, outperforming the state-of-the-art model CANConv [15] and recent diffusion-based methods PanDiff [33] and TMDiff [59]. As highlighted in the red box, our approach successfully restores challenging highly-uncertain regions, such as cars, where other models fall short.

Abstract

Conventional methods for PAN-sharpening often struggle to restore fine details due to limitations in leveraging high-frequency information. Moreover, diffusion-based approaches lack sufficient conditioning to fully utilize Panchromatic (PAN) images and low-resolution multispectral (LRMS) inputs effectively. To address these challenges, we propose an uncertainty-aware knowledge distillation diffusion framework with details enhancement for PAN-sharpening, called U-Know-DiffPAN. The U-Know-DiffPAN incorporates uncertainty-aware knowledge distillation for effective transfer of feature details from our teacher model to a student one. The teacher model in our U-Know-DiffPAN captures frequency details through frequency selective attention, facilitating accurate reverse process learning. By conditioning the encoder on compact vector representations of PAN and LRMS and the decoder on Wavelet transforms, we enable rich frequency utilization. So, the high-capacity teacher model distills frequency-rich features into a lightweight student model aided by an uncertainty map. From this, the teacher model can guide the

student model to focus on difficult image regions for PAN-sharpening via the usage of the uncertainty map. Extensive experiments on diverse datasets demonstrate the robustness and superior performance of our U-Know-DiffPAN over very recent state-of-the-art PAN-sharpening methods.

1. Introduction

Satellite imagery plays a vital role in a wide range of applications, including environmental monitoring, surveillance, and mapping [2, 11, 16, 31, 71]. High-resolution multispectral (HRMS) images that combine high spatial and spectral fidelity are commonly generated using PAN-sharpening techniques, fusing low-resolution multispectral (LRMS) images with high-resolution (HR) panchromatic (PAN) images. The primary objective of PAN-sharpening is to retain the spatial detail of PAN images while preserving the spectral information of LRMS images. Recently, deep learning (DL)-based approaches have gained attraction in PAN-sharpening tasks, leveraging deep networks to perform end-to-end image regression. However, DL models are typically limited by the local receptive field of convolutional layers, which primarily focus on local patterns

[†]Co-corresponding authors (equal advising).

and fail to capture long-range dependencies. This limitation often leads to overly smooth outputs with reduced high-frequency details.

To overcome this limitation, generative models such as generative adversarial networks (GANs) [19] have been applied to PAN-sharpening, aiming to produce more realistic results. Despite their success, GANs [30, 32] pose additional challenges, including training instability, mode collapse, and artifact generation, which can degrade image quality. More recently, diffusion models [22, 40, 44, 58] have demonstrated strong performance across a variety of image generation and restoration tasks. In PAN-sharpening, diffusion-based methods [33, 59] have shown promise by using PAN and LRMS images as conditioning inputs. However, they are limited by simple conditioning strategies that do not fully utilize the complementary information provided by the PAN and LRMS inputs, thus leading to suboptimal restoration quality. Additionally, diffusion models often incur high computational costs and longer inference times compared to other DL-based methods, limiting their practical applicability.

To address these challenges, we propose U-Know-DiffPAN demonstrated in Fig. 2, a novel PAN-sharpening framework that incorporates an uncertainty-aware knowledge distillation (U-Know) strategy. Our framework is designed to fully leverage the frequency information in PAN and LRMS inputs while reducing computational costs. Our teacher model, is built to maximize information extraction from PAN and LRMS images by utilizing (i) a Feed Forward Attention (FFA) block in the encoder to capture compact vector representations of PAN and LRMS, and (ii) a High Quality Frequency Enhancement (HQFE) block in the decoder, composed of Fourier Transform Channel Attention (FTCA) and Stationary Wavelet Transform Cross Attention (SWTCA) modules. The FTCA enhances crucial frequency components through Fourier transform-based [55] attention, while the SWTCA incorporates high-frequency information from PAN and low-frequency information from LRMS into the decoder.

Our U-Know strategy leverages uncertainty-aware knowledge distillation by transferring the features from the teacher model to a light-weight student model. The teacher model denoises HRMS images along with an uncertainty map, identifying spatial regions where the prediction confidence is low. Then based of the U-Know strategy, the teacher model distills to the student model not only the frequency-aware features but also the uncertainty map to address spatial weaknesses in the teacher’s predictions. This approach leads to improved performance and reduced computational cost, making our U-Know-DiffPAN more effective and efficient for PAN-sharpening. Our contributions are summarized as follows:

- We *firstly* incorporate the uncertainty-aware knowledge

distillation into diffusion based PAN-sharpening with the guidance of pixel-wise restoration uncertainty and frequency-selective attention for details enhancement;

- Our teacher model leverages compact vector representations to enhance encoding efficiency and employs frequency selective attention in the decoder to refine frequency components for PAN-sharpening.
- We conduct extensive experiments on multiple datasets [12], including WV3, QB, and GF2, demonstrating state-of-the-art performance and surpassing very recent methods in PAN-sharpening with *large margins*.

2. Related Works

2.1. PAN-Sharpening

PAN-sharpening is a technique to fuse high-resolution (HR) panchromatic (PAN) images with low-resolution multispectral (LRMS) images to produce HR multispectral (HRMS) images. Traditional PAN-sharpening techniques are broadly categorized into three approaches: component substitution (CS) [9, 43], multi-resolution analysis (MRA) [1, 36], and variational optimization (VO) [4]. Modern PAN-sharpening methods primarily consist of CNN-based [15, 26, 50, 61], transformer-based [26, 72], and GAN-based [30, 32] models. LAGConv [26] introduces local-context adaptive convolutional kernels with a global harmonic bias mechanism. S2DBPN [68] uses a spatial-spectral dual back-projection network for effective PAN and LRMS fusion. DCPNet [72] establishes a transformer-based dual-task parallel framework to optimize reconstruction. CANConv [15] integrates a non-local adaptive convolution module, enhancing spatial adaptability and non-local self-similarity. Besides the methods cited above, there are many other DL-based methods for PAN-sharpening [10, 14, 18, 23, 24]. While deep learning (DL)-based methods can capture complex mappings, they encounter challenges. CNN-based approaches tend to produce overly smooth results due to local receptive field of convolution layers. GAN-based models, though capable of generating realistic textures, may suffer from instability and introduce unrealistic artifacts.

Diffusion-based approaches. Diffusion models (DMs) [22, 44] offer a promising alternative to conventional DL-based methods for image restoration [51, 58], iteratively refining noisy images through progressive denoising. Unlike GANs [19, 27], which can be prone to instability, DMs use iterative denoising steps with flexible conditioning, making them robust for tasks such as image restoration and PAN-sharpening. Recent diffusion-based PAN-sharpening models [33, 59] have shown significant advancements. PanDiff [33], however, employs a relatively simplistic conditioning approach that limits its ability to fully utilize the information from the input data, sometimes resulting in subopti-

mal restoration quality. In contrast, TMDiff [59] employs a complex conditioning mechanism, requiring an additional pretrained CLIP [38] text encoder, which adds unnecessary complexity without substantial performance gains. Our proposed framework, U-Know-DiffPAN, handles these limitations by integrating an advanced conditioning strategy that maximizes the use of input information. Specifically, our U-Know-DiffPAN conditions the encoder on compact vector representations of PAN and LRMS, while the decoder is conditioned on the stationary wavelet transform [34] of PAN and LRMS. This approach allows our U-Know-DiffPAN to effectively capture both frequency details and spatial fidelity, achieving superior restoration quality compared to existing diffusion-based methods.

2.2. Knowledge Distillation

Knowledge Distillation (KD) [21] is a well-known method for transferring knowledge from a large, model (teacher) to a smaller model (student), enabling deployment in resource-constrained settings while retaining performance. KD has demonstrated effectiveness across a range of computer vision tasks, including classification [8, 60, 69], object detection [25, 52, 63, 74], and image restoration [45, 62, 70]. However, previous KD methods, often fall short in tasks such as super-resolution [70], where capturing complicated detail is essential. This limitation arises because conventional KD student learns all regions equally, without focusing on areas that require concentrated learning. To address this, we propose uncertainty-aware knowledge distillation (U-Know), which introduces an uncertainty map into the distillation process. Our U-Know strategy informs the student of uncertain regions, areas the teacher model finds challenging to restore, enabling the student model to refine crucial details, thereby enhancing fidelity in both spatial and spectral domains.

3. Methods

3.1. Overview of U-Know-DiffPAN

Fig. 2 shows the overview of our U-Know-DiffPAN framework. The proposed U-Know-DiffPAN framework comprises a teacher network with frequency-selective attention (FSA-T) and a student network (FSA-S), designed within a knowledge distillation paradigm. PAN image \mathbf{I}_{PAN} and interpolated LRMS image $\mathbf{I}_{\text{MS}}^{\text{LR}}$ are inputted in concatenation to generate HRMS image $\mathbf{I}_{\text{MS}}^{\text{HR}}$. Both FSA-T and FSA-S are designed to predict the residuals as:

$$\mathbf{X}_0 = \mathbf{I}_{\text{MS}}^{\text{HR}} - \mathbf{I}_{\text{MS}}^{\text{LR}}. \quad (1)$$

Our framework operates in two main stages: (i) pre-training the FSA-T within a diffusion process to produce an initial prediction $\tilde{\mathbf{X}}_0$ alongside an uncertainty map $\hat{\theta}$ that identifies spatially weak regions; and (ii) training the FSA-S by

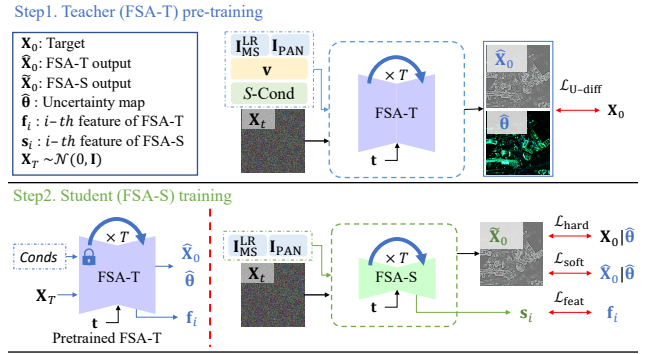


Figure 2. Overview of our uncertainty-aware knowledge-distillation diffusion framework with details enhancement, called U-Know-DiffPAN.

leveraging this uncertainty map to guide the FSA-S in refining these regions through the KD. In Sec. 3.2, we describe the FSA-T’s diffusion-based training process, which incorporates frequency information from PAN and LRMS inputs. Sec. 3.3 details the FSA-T architecture, specifically designed to enhance frequency components. Finally, in Sec. 3.4, we explain the FSA-S’s uncertainty-aware knowledge distillation framework, which utilizes the uncertainty map to achieve precise and reliable PAN-sharpening.

3.2. Diffusion Process of Teacher Network (FSA-T)

Diffusion models operate by defining a forward process that gradually adds noise to data until it becomes indistinguishable from random noise, and a reverse process that learns to denoise the data, reconstructing the original information. We leverage this framework into a frequency-selective attention teacher network (FSA-T) as our teacher network, to generate frequency enhanced HRMS images with their pixel-wise uncertainty information.

Forward process. In the forward diffusion process, noise is progressively added to the residual image, \mathbf{X}_0 , until it converges to a Gaussian distribution, $\mathbf{X}_T \sim \mathcal{N}(\mathbf{0}, \mathbf{I})$, after T timesteps. At each timestep $t \in \{1, \dots, T\}$, a noisy version of the residual is obtained as follows [22]:

$$\mathbf{X}_t = \sqrt{\bar{\alpha}_t} \mathbf{X}_0 + \sqrt{1 - \bar{\alpha}_t} \epsilon, \quad (2)$$

where $\epsilon \sim \mathcal{N}(\mathbf{0}, \mathbf{I})$ is Gaussian noise, and $\bar{\alpha}_t = \prod_{s=1}^t (1 - \beta_s)$ controls the noise level at step t .

Reverse process. Following the DDPM [22], the reverse process aims to recover \mathbf{X}_0 from \mathbf{X}_T by predicting a denoised image at each step. To perform denoising at each timestep, the denoising network (FSA-T), denoted as Ψ , is designed to predict the original \mathbf{X}_0 rather than the added noise ϵ , as we found this empirically to be beneficial for PAN-sharpening. Additionally, Ψ simultaneously produces an uncertainty map $\hat{\theta}$ for each prediction, providing pixel-

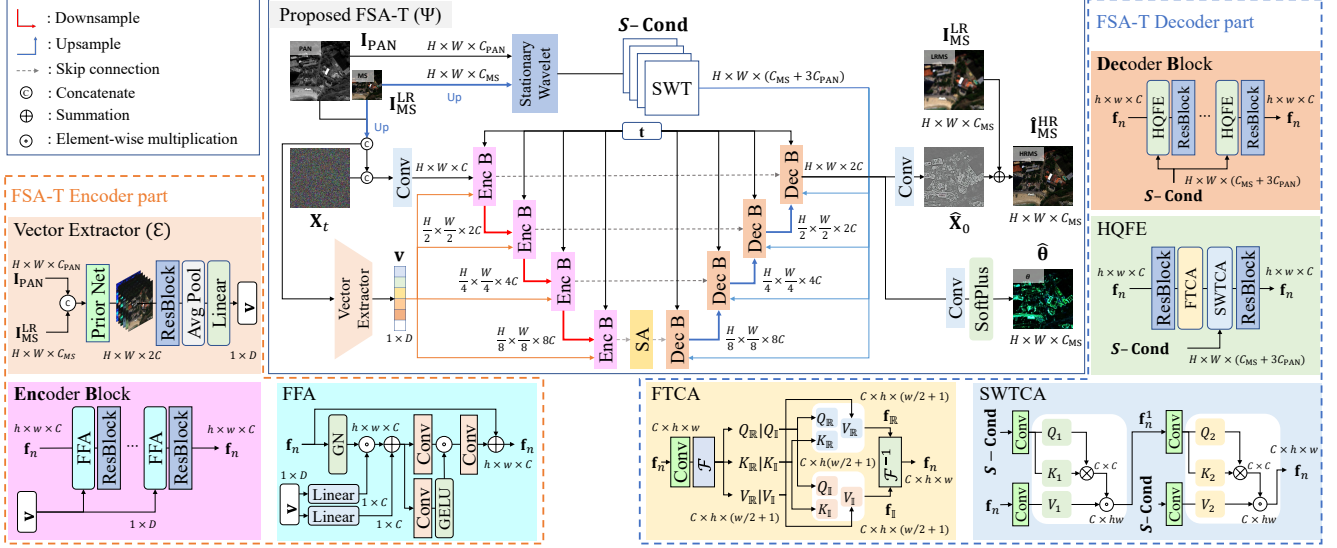


Figure 3. Architecture of our proposed teacher model with frequency-selective attention, denoted as FSA-T, for PAN-sharpening. The FSA-T is designed to fully utilize frequency information for details enhancement from PAN and LRMS inputs (more details in *Supplemental*.)

wise confidence information as:

$$\left[\hat{\mathbf{X}}_0 \mid \hat{\boldsymbol{\theta}} \right] = \Psi \left(\left[\mathbf{X}_t \mid \mathbf{I}_{\text{PAN}} \mid \mathbf{I}_{\text{LRMS}}^{\text{LR}} \right]; \mathbf{v}, \mathcal{S}\text{-Cond}; t \right), \quad (3)$$

where $[\cdot \mid \cdot]$ indicates channel-wise concatenation, $\hat{\mathbf{X}}_0$ is a predicted residual, $\hat{\boldsymbol{\theta}}$ is a predicted uncertainty map, \mathbf{v} and $\mathcal{S}\text{-Cond}$ represent a learning compact representation (vector) and Stationary Wavelet Transform (SWT)-based conditioning terms, respectively. This formulation allows the FSA-T to iteratively refine the noisy input, guided by the conditioned information (\mathbf{v} , $\mathcal{S}\text{-Cond}$), toward an accurate reconstruction of the \mathbf{X}_0 . $\hat{\boldsymbol{\theta}}$ captures pixel-wise prediction confidence, which guides the FSA-S to more rigorously learn the regions with high uncertainty. To ensure positivity, we apply the SoftPlus [73] activation to $\hat{\boldsymbol{\theta}}$.

Uncertainty-driven diffusion loss. Inspired by [35, 41], we employ the following uncertainty-driven diffusion loss function, $\mathcal{L}_{\text{U-Diff}}$, to optimize the teacher network Ψ :

$$\mathcal{L}_{\text{U-Diff}} = \left\| \frac{1}{2\hat{\boldsymbol{\theta}}} \odot \left| \hat{\mathbf{X}}_0 - \mathbf{X}_0 \right| + \frac{1}{2} \log \hat{\boldsymbol{\theta}} \right\|_1, \quad (4)$$

where $\hat{\boldsymbol{\theta}}$ serves as the estimated variance term and is regarded as the uncertainty map in our framework. This objective function encourages the model to minimize prediction errors in low-confidence regions, thus yielding a more accurate and spatially robust output.

3.3. Details of Teacher Network Architecture

Our teacher network, FSA-T, is designed to enhance frequency details for PAN-sharpening tasks by fully utilizing complementary information from PAN and LRMS inputs. The FSA-T adopts an encoder-decoder (U-Net [39]) structure, where each stage is specifically tailored to capture and

refine critical spatial and frequency features. The encoder of FSA-T employs Feed Forward Attention (FFA) blocks to extract compact and informative representations from the PAN and LRMS inputs. This attention mechanism allows the encoder to focus on essential features, preparing the data for effective frequency enhancement in subsequent layers.

The decoder of FSA-T integrates High-Quality Frequency Enhancement (HQFE) blocks at each decoding level to further refine frequency components. Each HQFE block comprises two key modules: Fourier Transform Channel Attention (FTCA) that emphasizes important frequency components via Fourier Transform based attention, and Stationary Wavelet Transform Cross Attention (SWTCA) that merges high-frequency information from PAN and low-frequency content from LRMS, both of which are decomposed by SWT [34]. By incorporating these specialize components, FSA-T effectively produces $\hat{\mathbf{X}}_0$ with enhanced spatial fidelity, establishing an effective uncertainty-aware knowledge distillation (U-Know) strategy.

Feed Forward Attention (FFA). The FFA block in Fig. 3 is designed to leverage compact information [58] from the PAN and LRMS input to establish a rough structural representation during encoding. A compact vector representation $\mathbf{v} \in \mathbb{R}^{1 \times D}$ is obtained by a vector extractor \mathcal{E} as:

$$\mathbf{v} = \mathcal{E} \left(\mathbf{I}_{\text{PAN}}, \mathbf{I}_{\text{LRMS}}^{\text{LR}} \right). \quad (5)$$

\mathbf{v} is then used as a dynamic modulation [27, 53] parameter within the FFA, enabling \mathcal{E} to incorporate \mathbf{v} and establish an approximate structure during restoration as follows:

$$\begin{aligned} [\beta_n \mid \gamma_n] &= \text{Linear}(\mathbf{v}), \\ \mathbf{f}'_n &= \gamma_n \odot \text{GN}(\mathbf{f}_n) + \beta_n, \\ \mathbf{f}_n &\leftarrow \text{Conv}(\mathbf{f}'_n) \odot \text{GELU}(\text{Conv}(\mathbf{f}'_n)) + \mathbf{f}_n, \end{aligned} \quad (6)$$

where $\mathbf{f}_n \in \mathbb{R}^{C \times h \times w}$ denotes input feature for the n -th encoder, Linear indicates Linear operation, \odot denotes element-wise multiplication, GN indicates group normalization [57], GELU indicates GELU [20] activation and Conv consists of a sequential 1×1 convolution and a 3×3 depth-wise convolution layer (Details of \mathcal{E} is in the *Supplemental*).

Fourier Transform Channel Attention (FTCA). The FTCA block in Fig. 3 performs self-attention in frequency domain by leveraging the 2D Fast Fourier Transform (FFT), denoted as \mathcal{F} . \mathcal{F} allows for efficient identification and emphasis of critical frequency components. For the n -th decoder block in Fig. 3, the input feature $\mathbf{f}_n \in \mathbb{R}^{C \times h \times w}$ of C channels is transformed into query (\mathbf{Q}), key (\mathbf{K}), and value (\mathbf{V}) representations. The 2D FFT \mathcal{F} is then applied independently to each channel of \mathbf{Q} , \mathbf{K} , and \mathbf{V} , mapping them transform from time domain to frequency domain as:

$$[\mathbf{Q} \mid \mathbf{K} \mid \mathbf{V}] = \mathcal{F}(\text{Conv}(\mathbf{f}_n)), \quad (7)$$

where \mathbf{Q} , \mathbf{K} and \mathbf{V} reside in $\mathbb{C}^{C \times h \times (\frac{w}{2} + 1)}$ due to the Hermitian symmetry property [6]. Note that each frequency domain representation of \mathbf{Q} , \mathbf{K} , and \mathbf{V} includes real and imaginary parts. So, we decompose \mathbf{Q} , \mathbf{K} , and \mathbf{V} into real and imaginary parts as:

$$[\mathbf{Q}_\mathbb{R} \mid \mathbf{K}_\mathbb{R} \mid \mathbf{V}_\mathbb{R}] + j[\mathbf{Q}_\mathbb{I} \mid \mathbf{K}_\mathbb{I} \mid \mathbf{V}_\mathbb{I}] = [\mathbf{Q} \mid \mathbf{K} \mid \mathbf{V}], \quad (8)$$

where $j = \sqrt{-1}$, and $\mathbf{Q}_\mathbb{R}$, $\mathbf{K}_\mathbb{R}$, $\mathbf{V}_\mathbb{R}$, $\mathbf{Q}_\mathbb{I}$, $\mathbf{K}_\mathbb{I}$, $\mathbf{V}_\mathbb{I}$ are in $\mathbb{R}^{C \times h \times (\frac{w}{2} + 1)}$. Self-attention operations are then performed separately on the real and imaginary parts as follows:

$$\mathbf{f}_l = \text{SoftMax}\left(\mathbf{Q}_l \mathbf{K}_l^\top / \sqrt{C}\right) \mathbf{V}_l, \quad (9)$$

where $l \in \{\mathbb{R}, \mathbb{I}\}$ indicates the real or imaginary feature, respectively. Finally, the inverse Fourier Transform \mathcal{F}^{-1} is applied to $\mathbf{f}_\mathbb{R}$ and $\mathbf{f}_\mathbb{I}$ to map them back to the time domain:

$$\mathbf{f}_n \leftarrow \mathcal{F}^{-1}(\mathbf{f}_\mathbb{R} + j\mathbf{f}_\mathbb{I}). \quad (10)$$

This process ensures that refined frequency information be selectively captured and utilized.

Stationary Wavelet Transform Cross Attention (SWTCA). The SWTCA block is designed to leverage Wavelet components of \mathbf{I}_{PAN} and $\mathbf{I}_{\text{MS}}^{\text{LR}}$ motivated by [37, 42, 75]. As shown in Fig. 3, it enhances the features outputted by the FTCA block, utilizing the Stationary Wavelet Transform (SWT) [34], denoted as \mathcal{S} . The SWTCA block selectively incorporates relevant frequency components from \mathbf{I}_{PAN} and $\mathbf{I}_{\text{MS}}^{\text{LR}}$ through a two-stage cross-attention process. The SWT-based conditioning terms ($\mathcal{S}\text{-Cond}$) are constructed by decomposing \mathbf{I}_{PAN} and $\mathbf{I}_{\text{MS}}^{\text{LR}}$ using \mathcal{S} into four components:

$$\begin{aligned} [\mathbf{L}_{\text{PAN}} \mid \mathbf{H}_{\text{PAN}} \mid \mathbf{V}_{\text{PAN}} \mid \mathbf{D}_{\text{PAN}}] &= \mathcal{S}(\mathbf{I}_{\text{PAN}}), \\ [\mathbf{L}_{\text{MS}}^{\text{LR}} \mid \mathbf{H}_{\text{MS}}^{\text{LR}} \mid \mathbf{V}_{\text{MS}}^{\text{LR}} \mid \mathbf{D}_{\text{MS}}^{\text{LR}}] &= \mathcal{S}(\mathbf{I}_{\text{MS}}^{\text{LR}}), \end{aligned} \quad (11)$$

where \mathbf{L} represent the low-frequency approximation components, while \mathbf{H} , \mathbf{V} , \mathbf{D} denote the high-frequency horizontal, vertical, and diagonal details, respectively. Since \mathbf{I}_{PAN} provides high spatial resolution but lacks spectral information, only its high-frequency components \mathbf{H}_{PAN} , \mathbf{V}_{PAN} , and \mathbf{D}_{PAN} are used. Conversely, $\mathbf{L}_{\text{MS}}^{\text{LR}}$ from $\mathbf{I}_{\text{MS}}^{\text{LR}}$ contains richer spectral information. These components are concatenated channel-wise to form $\mathcal{S}\text{-Cond}$ as:

$$\mathcal{S}\text{-Cond} = [\mathbf{L}_{\text{MS}}^{\text{LR}} \mid \mathbf{H}_{\text{PAN}} \mid \mathbf{V}_{\text{PAN}} \mid \mathbf{D}_{\text{PAN}}]. \quad (12)$$

To inject $\mathcal{S}\text{-Cond}$ into the feature \mathbf{f}_n obtained from FTCA at the n -th decoder block, we employ a two-stage cross-attention process. In the first stage, \mathbf{Q}_1 and \mathbf{K}_1 are derived from $\mathcal{S}\text{-Cond}$, directing attention toward critical frequency components, while \mathbf{V}_1 is derived from \mathbf{f}_n . The resulting features are reshaped to $C \times hw$ for channel attention [66], producing an intermediate feature $\mathbf{f}_n^1 \in \mathbb{R}^{C \times h \times w}$ as:

$$\begin{aligned} [\mathbf{Q}_1 \mid \mathbf{K}_1] &= \text{Conv}(\mathcal{S}\text{-Cond}), \quad \mathbf{V}_1 = \text{Conv}(\mathbf{f}_n), \\ \mathbf{f}_n^1 &= \text{SoftMax}\left(\mathbf{Q}_1 \mathbf{K}_1^\top / \sqrt{C}\right) \mathbf{V}_1, \end{aligned} \quad (13)$$

where \mathbf{Q}_1 , \mathbf{K}_1 , \mathbf{V}_1 are in $\mathbb{R}^{C \times hw}$. In the second stage, \mathbf{Q}_2 is derived from the intermediate feature \mathbf{f}_n^1 , while \mathbf{K}_2 and \mathbf{V}_2 come from $\mathcal{S}\text{-Cond}$, enabling the model to refine the correlation between the reconstructed feature \mathbf{f}_n and significant frequency components in $\mathcal{S}\text{-Cond}$. This stage yields the final feature $\mathbf{f}_n \in \mathbb{R}^{C \times h \times w}$ after reshaping:

$$\begin{aligned} \mathbf{Q}_2 &= \text{Conv}(\mathbf{f}_n^1), \quad [\mathbf{K}_2 \mid \mathbf{V}_2] = \text{Conv}(\mathcal{S}\text{-Cond}), \\ \mathbf{f}_n &\leftarrow \text{SoftMax}\left(\mathbf{Q}_2 \mathbf{K}_2^\top / \sqrt{C}\right) \mathbf{V}_2. \end{aligned} \quad (14)$$

Through these two stages of cross-attention, the final feature \mathbf{f}_n effectively incorporates essential frequency components from both PAN and MS inputs, ensuring enhanced frequency representation and high-quality HRMS output.

3.4. Uncertainty-Aware Knowledge Distillation

To address the substantial computational demands of the teacher (FSA-T) Ψ , we propose an novel uncertainty-aware knowledge distillation (U-Know) strategy.

Student network (FSA-S) ψ . The student model FSA-S is designed with the same number of encoder and decoder blocks as FSA-T. Each block consists solely of Res-blocks, and unlike the teacher, the student operates without any additional conditional inputs. As shown in Fig. 2, the lightweight student model ψ predicts the denoised image $\tilde{\mathbf{X}}_0$ from the input \mathbf{X}_t at timestep t as:

$$\tilde{\mathbf{X}}_0 = \psi([\mathbf{X}_t \mid \mathbf{I}_{\text{PAN}} \mid \mathbf{I}_{\text{MS}}^{\text{LR}}]; t). \quad (15)$$

U-Know loss function. FSA-T Ψ generates an uncertainty map $\hat{\theta}$ along with the output $\tilde{\mathbf{X}}_0$ during training.

These two outputs are frozen and used in the U-Know loss function, $\mathcal{L}_{\text{U-Know}}$, to train the FSA-S ψ . The total training objective combines a hard loss ($\mathcal{L}_{\text{hard}}$), a soft loss ($\mathcal{L}_{\text{soft}}$), and a feature loss ($\mathcal{L}_{\text{feat}}$) to distill frequency-rich features and enhance regions where Ψ exhibits spatial weaknesses points. The total loss is defined as:

$$\mathcal{L}_{\text{U-Know}} = \mathcal{L}_{\text{hard}} + \lambda_s \mathcal{L}_{\text{soft}} + \lambda_f \mathcal{L}_{\text{feat}}, \quad (16)$$

where λ_s and λ_f control the contributions of $\mathcal{L}_{\text{soft}}$ and $\mathcal{L}_{\text{feat}}$, respectively. $\mathcal{L}_{\text{hard}}$ measures the difference between ψ output $\tilde{\mathbf{X}}_0$ and the ground truth \mathbf{X}_0 , weighted by Ψ 's uncertainty map $\hat{\theta}$ to emphasize challenging regions:

$$\mathcal{L}_{\text{hard}} = \left\| (\tau + \hat{\theta}) \odot \left| \tilde{\mathbf{X}}_0 - \mathbf{X}_0 \right| \right\|_1, \quad (17)$$

where τ is a hyper-parameter. $\mathcal{L}_{\text{soft}}$ computes the difference between ψ 's output $\tilde{\mathbf{X}}_0$ and Ψ 's output $\hat{\mathbf{X}}_0$, weighted by the $\hat{\theta}$ to help ψ better approximate the Ψ 's knowledge:

$$\mathcal{L}_{\text{soft}} = \left\| (\tau - \hat{\theta}) \odot \left| \tilde{\mathbf{X}}_0 - \hat{\mathbf{X}}_0 \right| \right\|_1. \quad (18)$$

In the regions where $\hat{\theta}$ values are high, indicating that Ψ struggles with the task, we apply a weight of $(\tau + \hat{\theta})$ and use \mathbf{X}_0 as the hard ground truth to guide ψ toward the true target. Conversely, in the areas where $\hat{\theta}$ values are low, indicating that Ψ performs well, we apply a weight of $(\tau - \hat{\theta})$ and use Ψ 's output $\hat{\mathbf{X}}_0$ as the soft ground truth, allowing ψ to approximate Ψ 's knowledge in these regions. These dual loss formulations enable Ψ to focus on challenging areas while effectively leveraging the Ψ 's strengths. $\mathcal{L}_{\text{feat}}$ ensures alignment between intermediate features of Ψ and ψ as [5]:

$$\ell_{\text{feat}}^i = \sqrt{\|\mathbf{f}_i - \mathbf{s}_i\|_1^2 + \gamma}, \quad \mathcal{L}_{\text{feat}} = \sum_i \alpha_i \ell_{\text{feat}}^i, \quad (19)$$

where ℓ_{feat}^i is a feature loss for the i -th feature, α_i is a weight for the i -th feature, and \mathbf{f}_i and \mathbf{s}_i denote the i -th intermediate feature maps of Ψ and ψ respectively. The small constant γ ensures smooth convergence during optimization.

4. Experiment

4.1. Datasets, Metrics and Training Details

Satellite		WorldView-3	QuickBird	GaoFen-2
Number of Band		8	4	4
Spatial Resolution (m)	PAN	0.3	0.6	0.8
	LRMS	1.2	2.4	3.2
Radiometric Resolution (bit)		11	11	10
Number of (Train / Test) Images		9,714 / 20	17,139 / 20	19,809 / 20
Patch Size	PAN	64×64×1	64×64×1	64×64×1
	LRMS	16×16×8	16×16×4	16×16×4

Table 1. Detailed information of Worldview-3, QuickBird, and GaoFen-2 datasets.

Table 1 summarizes the characteristics of three datasets from PanCollection [12] for our experiments: WorldView-3 (WV3), QuickBird (QB), and GaoFen-2 (GF2). Data augmentation was performed using random vertical and horizontal flips. All experiments were conducted with a batch size of 32 for 300K iterations per dataset on an NVIDIA GeForce RTX 3090 GPU. The initial learning rate was set to 10^{-4} with a decay factor of 0.5 applied every 10K iterations, using the AdamW optimizer [13] with $\beta_1 = 0.9$, $\beta_2 = 0.999$, and a weight decay of 10^{-4} . For the diffusion process of our FSA-T and FSA-S, the total diffusion time step T was set to 500, with the DDIM [44] sampling strategy used to generate HRMS images in 25 steps. We set the hyper-parameters as $\lambda_s = 0.1$, $\lambda_f = 0.001$, $\tau = 1$, and $\alpha_i = 1$, which were empirically found to yield excellent performance. To evaluate the model performance, we employed widely accepted metrics that capture various aspects of image quality and similarity. For the reduced-resolution datasets of WV3, QB, and GF2, we used six standard metrics: PSNR [54], SSIM [54], SAM [65], ERGAS [49], SCC [17], and Q4/Q8 [47]. For the full-resolution datasets of WV3, QB, and GF2, we used HQNR [48] with D_λ , and D_S to comprehensively assess the results.

4.2. Experimental Results

To ensure a thorough and equitable evaluation, we used the official codes for each compared method whenever available. For methods without official codes, we re-implemented them based on the papers [33, 59] to maintain fairness in comparison.

Quantitative analysis. As shown in Table 2 and Table 3, our FSA-T achieves superior performance on the WV3, QB, and GF2 datasets compared to all other methods. The GF2 dataset contains relatively easier (less complex) images, so the teacher model can fully leverage its high-capacity features. In contrast, for the more challenging (more complex) WV3 and QB datasets, our FSA-S surpasses FSA-T across several metrics. This improvement represents the effectiveness of our uncertainty-aware knowledge distillation (U-Know) strategy, which enables the student model (FSA-S) to address the spatial weaknesses of the teacher model by focusing on uncertain regions. From this, the FSA-S can benefit more generalization from the knowledge distillation with uncertainty maps, leading to better performances than the FSA-T for the test datasets. Consequently, our FSA-S demonstrates an enhanced adaptability and robustness on complex datasets, where precise handling of spatial details (high frequency components) is essential.

Qualitative analysis. Fig. 4 shows the output HRMS images $\hat{\mathbf{I}}_{\text{MS}}^{\text{HR}}$ in the first rows and the error maps (MAE images) between $\hat{\mathbf{I}}_{\text{MS}}^{\text{HR}}$ and ground truth $\mathbf{I}_{\text{MS}}^{\text{HR}}$. As shown, our framework generates the results $\hat{\mathbf{I}}_{\text{MS}}^{\text{HR}}$ closer to $\mathbf{I}_{\text{MS}}^{\text{HR}}$ in the re-

GF2 Dataset			Reduced-Resolution						Full-Resolution		
Types	Methods	Publications	PSNR \uparrow	SSIM \uparrow	SAM \downarrow	ERGAS \downarrow	SCC \uparrow	Q4 \uparrow	$D_\lambda \downarrow$	$D_s \downarrow$	HQNR \uparrow
Non-DMs	PanNet [61]	ICCV 2017	39.197	0.959	1.050	1.038	0.975	0.963	0.020	0.052	0.929
	MSDCNN [64]	JSTARS 2018	40.730	0.971	0.946	0.862	0.983	0.972	0.026	0.079	0.898
	FusionNet [56]	ICCV 2021	39.866	0.966	0.971	0.960	0.980	0.967	0.034	0.105	0.865
	LAGConv [26]	AAAI 2022	41.147	0.974	0.886	0.816	0.985	0.974	0.030	0.078	0.895
	S2DBPN [68]	TGRS 2023	42.686	0.980	0.772	0.686	0.990	0.981	0.020	0.046	0.935
	DCPNet [72]	TGRS 2024	42.312	0.979	0.806	0.724	0.988	0.980	0.024	0.024	0.953
	CANConv [15]	CVPR 2024	43.166	0.982	0.722	0.653	0.991	0.983	0.019	0.063	0.919
Diffusion Models	PanDiff [33]	TGRS 2023	42.827	0.980	0.767	0.674	0.990	0.981	0.020	0.045	0.936
	TMDiff [59]	TGRS 2024	41.896	0.977	0.764	0.754	0.988	0.979	0.029	0.030	0.942
	FSA-S	Ours	44.585	0.986	0.624	0.548	0.993	0.987	0.018	0.037	0.944
	FSA-T	Ours	44.757	0.988	0.603	0.537	0.994	0.988	0.017	0.029	0.953

Table 2. Comparison of different models on the GaoFen-2 (GF2) dataset. **Blue** indicates the second-best performance, while **red** highlights the best-performing model. Standard deviations of the metrics across test samples are provided in the *Supplemental*.

Types	Methods	WV3 Dataset (Reduced-Resolution)						QB Dataset (Reduced-Resolution)					
		PSNR \uparrow	SSIM \uparrow	SAM \downarrow	ERGAS \downarrow	SCC \uparrow	Q8 \uparrow	PSNR \uparrow	SSIM \uparrow	SAM \downarrow	ERGAS \downarrow	SCC \uparrow	Q4 \uparrow
Non-DMs	PanNet [61]	36.148	0.966	3.402	2.538	0.979	0.913	35.563	0.939	5.273	4.856	0.966	0.911
	MSDCNN [64]	36.329	0.967	3.300	2.489	0.979	0.914	37.040	0.954	4.828	4.074	0.977	0.925
	FusionNet [56]	36.569	0.968	3.188	2.428	0.981	0.916	36.821	0.952	4.892	4.183	0.975	0.923
	LAGConv [26]	36.732	0.970	3.153	2.380	0.981	0.916	37.565	0.958	4.682	3.845	0.980	0.930
	S2DBPN [68]	37.216	0.972	3.019	2.245	0.985	0.917	37.314	0.956	4.849	3.956	0.980	0.928
	DCPNet [72]	37.009	0.972	3.083	2.301	0.984	0.915	38.079	0.963	4.420	3.618	0.983	0.935
	CANConv [15]	37.441	0.973	2.927	2.163	0.985	0.918	37.795	0.960	4.554	3.740	0.982	0.935
Diffusion Models	PanDiff [33]	37.029	0.971	3.058	2.276	0.984	0.913	37.842	0.959	4.611	3.723	0.982	0.935
	TMDiff [59]	37.477	0.973	2.885	2.151	0.986	0.915	37.642	0.958	4.627	3.804	0.981	0.930
	Our FSA-S	37.930	0.976	2.797	2.046	0.988	0.922	38.361	0.964	4.337	3.500	0.984	0.938
	Our FSA-T	37.894	0.976	2.801	2.055	0.987	0.921	38.343	0.964	4.349	3.502	0.985	0.938

Table 3. Performance comparison of different models on WV3 and QB datasets. **Red** and **blue** highlights the best- and 2nd-best performing models. The results for the full-resolution datasets and detailed results with standard deviations are provided in the *Supplemental*.

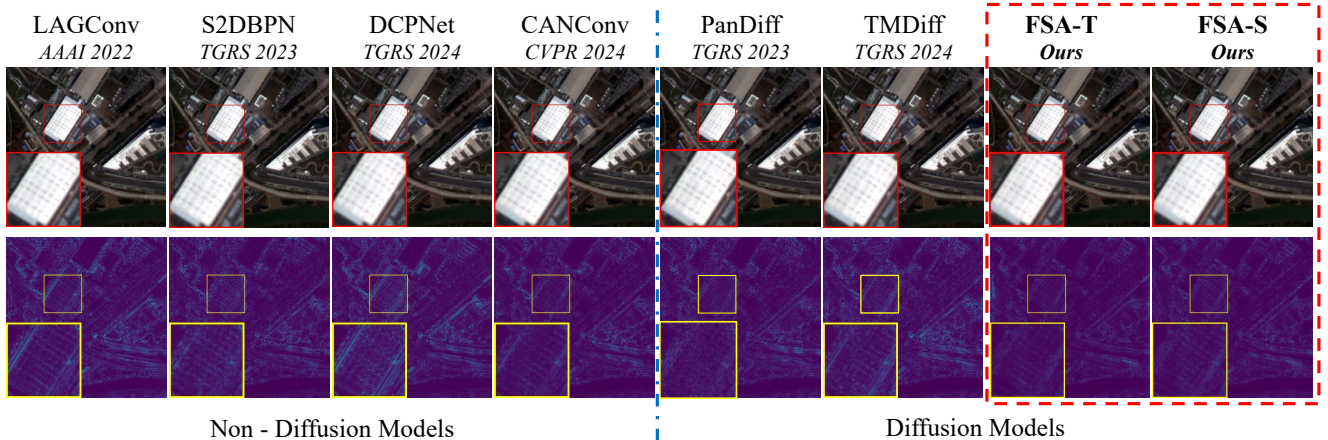


Figure 4. Visual comparison of PAN-sharpening results on the reduced-resolution GF2 dataset. The first row shows RGB of outputs \mathbf{I}_{MS}^{HR} , and the second row displays Error Map, the difference between output \mathbf{I}_{MS}^{HR} and ground truth \mathbf{I}_{MS}^{HR} . Both FSA-T and FSA-S achieve more detailed results compared to state-of-the-art models.

duced resolution GF2 data set. Furthermore, Fig. 1 demonstrates that even in the full-resolution comparison where ground truth is unavailable, our framework enables to generate more detailed and stable results compared to all other state-of-the-art approaches.

Computational complexity analysis. Table 4 compares

the computational cost of diffusion-based models, detailing parameters (Params.), floating-point operations (FLOPs), inference time (Time) and memory usage. This demonstrates the efficiency of our FSA-S over other models. In particular, the TMDiff has significantly higher numbers of parameters and FLOPs. The FSA-T, while computationally

Methods	Params. (M)	FLOPs (T)	Time (s)	Memory (GB)
PanDiff [33]	12.556	0.471	19.522	3.260
TMDiff [59]	153.939	5.517	67.461	10.483
FSA-T	25.492	1.402	25.495	5.910
FSA-S	9.115	0.346	12.287	2.136

Table 4. Computational complexity comparison for diffusion-based models. Best values are highlighted in **red**.

intensive than the FSA-S, still provides a balanced trade-off between efficiency and performance.

4.3. Ablation Studies

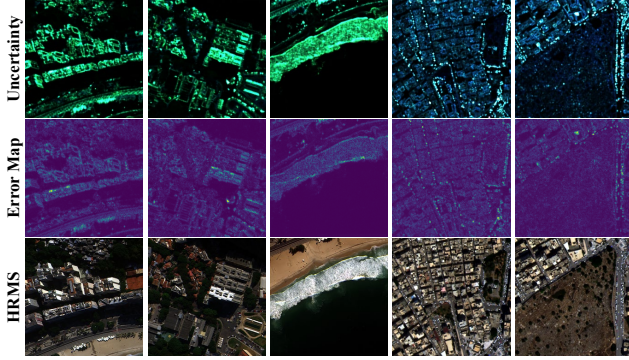


Figure 5. Visualization of uncertainty map $\hat{\theta}$, Error Map, and ground truth \mathbf{I}_{MS}^{HR} of reduced WV3.

Visualization of uncertainty map $\hat{\theta}$ of Ψ . The uncertainty map $\hat{\theta}$ learned through Eq. 4 shows that the areas with low uncertainty appear dark, while the areas with high uncertainty appear bright. Fig. 5 visualizes the uncertainty maps $\hat{\theta}$, error maps and ground truth \mathbf{I}_{MS}^{HR} for the reduced WV3 dataset. As shown in Fig. 5, it can be noted that the high-uncertainty regions mainly correspond to high-frequency areas such as challenging object edges. The learned uncertainty maps tend to resemble the error maps.

Encoder	Decoder	GF2 Dataset (Reduced-Resolution)			
		SAM↓	ERGAS↓	SCC↑	Q4↑
FFA	HQFE	0.654 ± 0.112	0.661 ± 0.076	0.992 ± 0.001	0.986 ± 0.007
✓		0.654 ± 0.112	0.636 ± 0.077	0.993 ± 0.002	0.986 ± 0.007
	✓	0.617 ± 0.117	0.556 ± 0.104	0.993 ± 0.002	0.987 ± 0.007
✓	✓	0.603 ± 0.102	0.537 ± 0.077	0.994 ± 0.001	0.988 ± 0.006

Table 5. Comparison of Results with and without FFA and HQFE Blocks in FSA-T. Best values are highlighted in **red**.

Effect of FFA, HQFE blocks in FSA-T. Table 5 presents the effectiveness of FFA and HQFE. As noted, there are a significant improvement across all metrics. The performance gains are much greater than when applying FFA to the encoder alone or HQFE to the decoder alone, as simultaneous condition injection creates a synergistic effect. The synergy of using both FFA and HQFE occurs because FFA sets up initial styles or "sketches" for \mathbf{I}_{MS}^{HR} images, followed by the decoder that restores frequency details via the HQFE.

This step-by-step learning process greatly benefits overall performance.

Loss func.	GF2 Dataset (Full-Resolution)		
	D_A ↓	D_s ↓	HQNR ↑
\mathcal{L}_1	0.026 ± 0.014	0.040 ± 0.017	0.935 ± 0.020
\mathcal{L}_{KD}	0.025 ± 0.015	0.038 ± 0.016	0.938 ± 0.021
\mathcal{L}_{U-know}	0.018 ± 0.011	0.037 ± 0.007	0.944 ± 0.012

Table 6. Impact of our U-know loss function design. Best values are highlighted in **red**.

Impact of the U-Know loss. To verify the effectiveness of our uncertainty-aware knowledge distillation loss \mathcal{L}_{U-know} (U-know loss), we trained the student model (FSA-S) using three losses: a widely used L_1 , a conventional knowledge distillation loss \mathcal{L}_{KD} which is same from our method \mathcal{L}_{U-know} but without considering the uncertainty map, and our \mathcal{L}_{U-know} . Table 6 shows the performance comparisons for the three losses. As shown, when the FSA-S was trained with \mathcal{L}_{U-know} , it achieved the best performance across all three metrics. This highlights the effectiveness of \mathcal{L}_{U-know} that enables the FSA-S to better leverage the teacher (FSA-T)’s prior knowledge including the uncertainty maps $\hat{\theta}$, output features \mathbf{f}_i , and output HRMS $\hat{\mathbf{I}}_{MS}^{HR}$ for improved learning.

4.4. Limitations

Inference time limitations. Despite U-Know-DiffPAN’s superior performance across multiple metrics, one notable limitation lies in its inference speed, compared to non-diffusion-based models. Diffusion models unavoidably require multiple sampling steps during inference, making this process inevitably slower. This iterative approach, while being beneficial for image generation of high quality, limits the model’s efficiency in real-time applications. Future work could focus on optimizing the inference process by pruning sampling steps, while maintaining performance.

5. Conclusion

We introduced U-Know-DiffPAN, a novel diffusion-based PAN-sharpening framework that effectively leverages frequency information from PAN and LRMS inputs to generate high-quality HRMS images. Our Uncertainty-aware Knowledge Distillation (U-Know) strategy enables efficient feature transfer by distilling both frequency-rich features and uncertainty maps from the teacher model, enhancing the restoration performance for spatially weak regions while reducing computational costs for the student model (FSA-S). Extensive experiments on multiple datasets, including WV3, QB, and GF2, demonstrate that our U-Know-DiffPAN outperforms very recent state-of-the-art methods in PAN-sharpening, establishing a new benchmark for performance and efficiency in satellite image processing.

A. More Details of Methods

A.1. Details of Vector Extractor

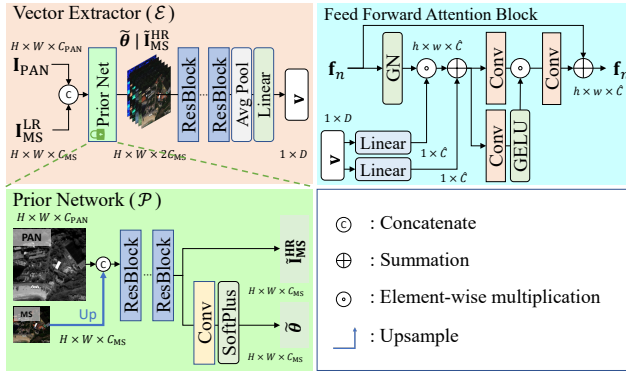


Figure 6. Detailed structure of Vector Extractor (\mathcal{E}). The simple representation of \mathcal{E} is presented in Fig. 3 of the main paper.

The detailed structure of the Vector Extractor \mathcal{E} in Fig. 3 of the main paper is depicted in Fig. 6 and Eq. 20, which extracts a compact vector representation $\mathbf{v} \in \mathbb{R}^{1 \times D}$ from two inputs: \mathbf{I}_{PAN} and $\mathbf{I}_{\text{MS}}^{\text{LR}}$. \mathcal{E} leverages a pretrained lightweight prior network \mathcal{P} that takes \mathbf{I}_{PAN} and $\mathbf{I}_{\text{MS}}^{\text{LR}}$ as inputs to generate a prior HRMS $\tilde{\mathbf{I}}_{\text{MS}}^{\text{HR}}$ and a prior uncertainty map $\tilde{\boldsymbol{\theta}}$. These outputs, $\tilde{\mathbf{I}}_{\text{MS}}^{\text{HR}}$ and $\tilde{\boldsymbol{\theta}}$, are then processed through multiple ResBlocks, followed by average pooling and a linear layer, to produce the final compact vector representation \mathbf{v} .

$$\begin{aligned} \left[\tilde{\boldsymbol{\theta}} \mid \tilde{\mathbf{I}}_{\text{MS}}^{\text{HR}} \right] &= \mathcal{P} \left(\mathbf{I}_{\text{PAN}}, \mathbf{I}_{\text{MS}}^{\text{LR}} \right), \\ \mathbf{v} &= \text{Linear} \left(\text{AvgPool} \left(\text{ResBlock}^n \left(\left[\tilde{\boldsymbol{\theta}} \mid \tilde{\mathbf{I}}_{\text{MS}}^{\text{HR}} \right] \right) \right) \right). \end{aligned} \quad (20)$$

where $\tilde{\boldsymbol{\theta}}$ denotes prior uncertainty map and $\tilde{\mathbf{I}}_{\text{MS}}^{\text{HR}}$ is prior HRMS obtained from prior network \mathcal{P} . The compact vector representation \mathbf{v} not only encapsulates the combined information from \mathbf{I}_{PAN} and $\mathbf{I}_{\text{MS}}^{\text{LR}}$, but also integrates the uncertainty information $\tilde{\boldsymbol{\theta}}$ derived from the prior network \mathcal{P} . This representation is subsequently used as a conditioning input to the Feed Forward Attention (FFA) block in the encoder blocks of FSA-T.

A.2. Fourier Transform Channel Attention (FTCA)

The detailed structure of FTCA in Fig. 3 of the main paper is depicted in Fig. 7, which is designed to enhance frequency domain features by applying the Discrete Fourier Transform (DFT) to feature maps, allowing self-attention to be performed more effectively in the frequency domain. As shown in Fig. 7, the input feature map is first transformed from the time domain to the frequency domain using 2D DFT. The real and imaginary parts of the 2D DFT feature map are then processed separately using channel attention. After applying channel attention to both real and

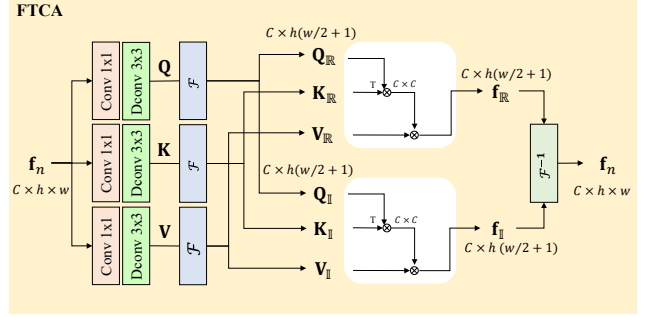


Figure 7. Detailed structure of Fourier Transform Channel Attention (FTCA) block. The simple representation of FTCA is presented in Fig. 3 of the main paper.

imaginary parts, the Inverse Fourier Transform is applied to bring the features back into the time domain, producing the enhanced output. This transform-domain self attention facilitates more effective computations of frequency components to selectively emphasize. This process ensures that high-quality frequency information be effectively captured and utilized, resulting in enhanced feature representation and improved model performance.

A.3. Stationary Wavelet Transform Cross Attention (SWTCA)

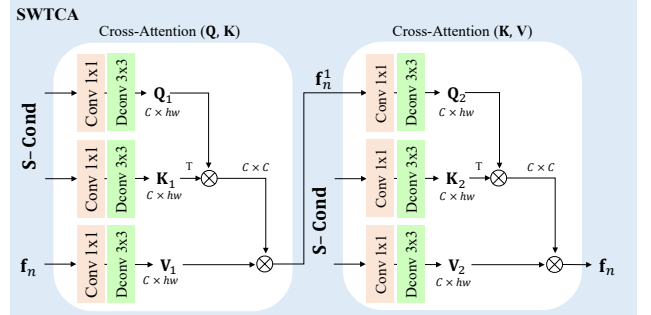


Figure 8. Detailed structure of our Stationary Wavelet Transform Cross Attention (SWTCA) block. The simple representation of SWTCA is presented in Fig. 3 of the main paper.

Following the approach of ResDiff [42], WaveDiff [37], and WINet [67], the SWTCA in Fig. 3 of the main paper is detailed in Fig. 8, which utilizes wavelet components of PAN and MS images decomposed using the Stationary Wavelet Transform (SWT). The SWTCA block is designed to inject additional frequency information into the features \mathbf{f}_n enhanced by the preceding FTCA. It selectively incorporates useful frequency components derived from the \mathbf{I}_{PAN} and $\mathbf{I}_{\text{MS}}^{\text{LR}}$ using the SWT while maintaining shift invariance as conditions for our Diffusion Model Ψ . The outputs of SWT for \mathbf{I}_{PAN} and $\mathbf{I}_{\text{MS}}^{\text{LR}}$ are constructed respectively as fol-

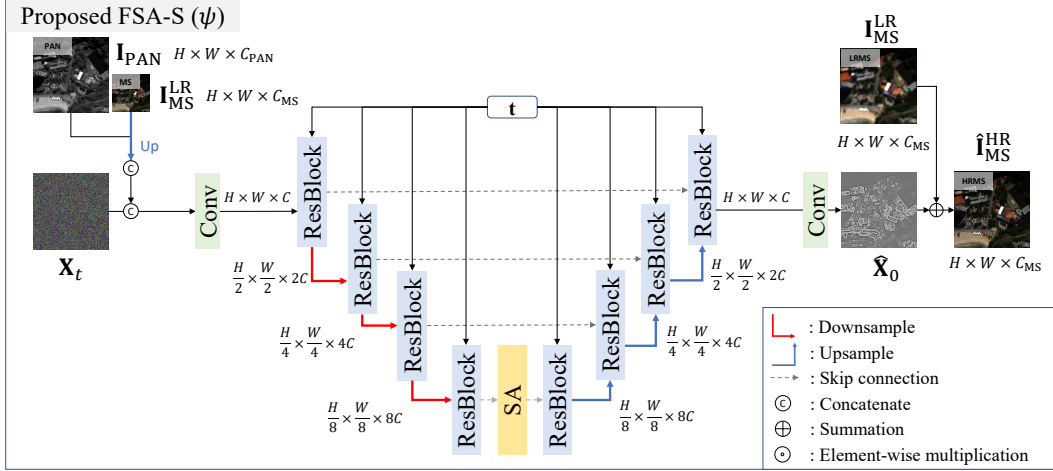


Figure 9. Detailed structure of FSA-S ψ .

lows:

$$\begin{aligned} \mathcal{S}(\mathbf{I}_{\text{PAN}}) &= [\mathbf{L}_{\text{PAN}} \mid \mathbf{H}_{\text{PAN}} \mid \mathbf{V}_{\text{PAN}} \mid \mathbf{D}_{\text{PAN}}], \\ \mathcal{S}(\mathbf{I}_{\text{MS}}^{\text{LR}}) &= [\mathbf{L}_{\text{MS}}^{\text{LR}} \mid \mathbf{H}_{\text{MS}}^{\text{LR}} \mid \mathbf{V}_{\text{MS}}^{\text{LR}} \mid \mathbf{D}_{\text{MS}}^{\text{LR}}], \end{aligned} \quad (21)$$

where \mathbf{L} represent the low-frequency approximation components, while \mathbf{H} , \mathbf{V} , \mathbf{D} denote the high-frequency horizontal, vertical, and diagonal details, respectively. Since \mathbf{I}_{PAN} provides highly detailed texture from its high spatial resolution but lacks spectral information, only its high-frequency components, which include \mathbf{H}_{PAN} , \mathbf{V}_{PAN} and \mathbf{D}_{PAN} , are used. Conversely, $\mathbf{L}_{\text{MS}}^{\text{LR}}$ from $\mathbf{I}_{\text{MS}}^{\text{LR}}$ contains richer spectral information. So, these components are concatenated channel-wise to form $\mathcal{S}\text{-Cond}$ that is the condition to be inputted to Ψ . $\mathcal{S}\text{-Cond}$ is then constructed as follows:

$$\mathcal{S}\text{-Cond} = [\mathbf{L}_{\text{MS}}^{\text{LR}} \mid \mathbf{H}_{\text{PAN}} \mid \mathbf{V}_{\text{PAN}} \mid \mathbf{D}_{\text{PAN}}]. \quad (22)$$

Note that the construction of this kind condition is motivated from the traditional MRA(Multi-Resolution Analysis)-based [1, 36, 75] PAN-sharpening methods that have utilized high-frequency Wavelet components of \mathbf{I}_{PAN} and low-frequency Wavelet components of $\mathbf{I}_{\text{MS}}^{\text{LR}}$. To inject $\mathcal{S}\text{-Cond}$ into the feature \mathbf{f}_n obtained from FTCA at the n -th decoder block, we employ a two-stage cross-attention process. In the first stage, \mathbf{Q}_1 and \mathbf{K}_1 are derived from $\mathcal{S}\text{-Cond}$, directing attention toward important frequency components, while \mathbf{V}_1 is derived from \mathbf{f}_n . The resulting intermediate feature $\mathbf{f}_n^1 \in \mathbb{R}^{C \times h \times w}$ is given as:

$$\begin{aligned} [\mathbf{Q}_1 \mid \mathbf{K}_1] &= \text{Conv}(\mathcal{S}\text{-Cond}), \quad \mathbf{V}_1 = \text{Conv}(\mathbf{f}_n), \\ \mathbf{f}_n^1 &= \text{SoftMax}\left(\frac{\mathbf{Q}_1 \mathbf{K}_1^T}{\sqrt{C}}\right) \mathbf{V}_1, \end{aligned} \quad (23)$$

where \mathbf{Q}_1 , \mathbf{K}_1 , $\mathbf{V}_1 \in \mathbb{R}^{C \times hw}$ are a Query, a Key and a Value, respectively. The \mathbf{Q}_1 , \mathbf{K}_1 and \mathbf{V}_1 are reshaped to

$C \times hw$ for channel attention. In the second stage, \mathbf{Q}_2 is derived from the intermediate feature \mathbf{f}_n^1 , while \mathbf{K}_2 and \mathbf{V}_2 come from $\mathcal{S}\text{-Cond}$, enabling the model to refine the correlation between the reconstructed feature \mathbf{f}_n and the frequency components in $\mathcal{S}\text{-Cond}$. This stage yields the final feature $\mathbf{f}_n \in \mathbb{R}^{C \times h \times w}$ after reshaping \mathbf{Q}_2 , \mathbf{K}_2 and \mathbf{V}_2 into $C \times hw$ for channel attention, which is given as follows:

$$\begin{aligned} \mathbf{Q}_2 &= \text{Conv}(\mathbf{f}_n^1), \quad [\mathbf{K}_2 \mid \mathbf{V}_2] = \text{Conv}(\mathcal{S}\text{-Cond}), \\ \mathbf{f}_n &\leftarrow \text{SoftMax}\left(\frac{\mathbf{Q}_2 \mathbf{K}_2^T}{\sqrt{C}}\right) \mathbf{V}_2. \end{aligned} \quad (24)$$

The first cross-attention block in Fig. 8 uses both Query and Key mappings from $\mathcal{S}\text{-Cond}$, focusing the attention map purely on $\mathcal{S}\text{-Cond}$ information, and aiding in concentrating on the significant channels of the feature \mathbf{f}_n . The second cross-attention block in Fig. 8 uses Query from the intermediate feature \mathbf{f}_n^1 and Key from $\mathcal{S}\text{-Cond}$, learning the correlation between the reconstructed feature \mathbf{f}_n^1 and the meaningful frequency information in \mathbf{I}_{PAN} and $\mathbf{I}_{\text{MS}}^{\text{LR}}$. This block helps emphasizing significant frequency components within $\mathcal{S}\text{-Cond}$.

A.4. Student network FSA-S (ψ) architecture

The student model, denoted as FSA-S ψ , is a diffusion-based model designed with the same number of encoder and decoder blocks as FSA-T Ψ . Each block consists solely of ResBlocks, and unlike the teacher Ψ , the FSA-S operates without any additional conditional inputs. As shown in Fig.2, the lightweight FSA-S ψ predicts denoised image $\tilde{\mathbf{X}}_0$ from input \mathbf{X}_t at timestep t as:

$$\tilde{\mathbf{X}}_0 = \psi([\mathbf{X}_t \mid \mathbf{I}_{\text{PAN}} \mid \mathbf{I}_{\text{MS}}^{\text{LR}}]; t). \quad (25)$$

B. Stationary Wavelet Transform compared to Discrete Wavelet Transform

Discrete Wavelet transforms have been widely used in image processing and PAN-sharpening tasks due to their ability to analyze signals across multiple resolutions. Discrete Wavelet Transform (DWT) decomposes signals into low-frequency (approximation) and high-frequency (detail) components at each level. Although DWT has proven to be effective in numerous applications, it suffers from shift variance due to its inherent downsampling operation at each decomposition level. To address this limitation, the Stationary Wavelet Transform (SWT) was introduced. Unlike DWT, SWT omits the downsampling step, ensuring that the signal size remains constant across all levels. This design enables SWT to maintain shift invariance, meaning that minor shifts in the input signal do not affect the transformation results. This property makes SWT highly advantageous in applications such as PAN-sharpening, where maintaining consistency in transformed results is crucial. Specifically, SWT ensures that the wavelet coefficients remain stable even when the input signal undergoes small translations, leading to more robust performance in PAN-sharpening tasks. In addition, SWT allows for higher resolution analysis across all levels, as the image or signal is not downsampled during the transformation. Compared to DWT that inherently reduces the image resolutions at each level, SWT retains the original resolution, making it more suitable for tasks that require detailed frequency information.

B.1. SWT condition versus DWT condition

Condition	GF2 Dataset (Reduced-Resolution)			
	SAM↓	ERGAS↓	SCC↑	Q4↑
DWT	0.646 ± 0.117	0.567 ± 0.095	0.993 ± 0.002	0.987 ± 0.007
SWT	0.603 ± 0.102	0.537 ± 0.077	0.994 ± 0.001	0.988 ± 0.006

Table 7. Comparison of results between DWT and SWT conditioning at the SWTCA block in FSA-T Ψ , with the best values highlighted in red.

Table 7 represents the performance differences between DWT and SWT for the \mathcal{S} -Cond in Eq. 22 as the conditioning input to the SWTCA block in FSA-T Ψ . The SWT-based \mathcal{S} -Cond outperforms the DWT-based one across all metrics. The results in Table 7 highlight that SWT achieves lower SAM and ERGAS values, as well as higher SCC and Q4 scores, indicating its superior performance in PAN-sharpening tasks. This improvement underscores the advantages of shift invariance and resolution preservation provided by SWT.

C. Uncertainty Estimation

Uncertainty estimation has been an important topic of research in deep learning. Several works [3, 29, 41, 46]

have incorporated uncertainty into regression problems. A Bayesian deep learning framework was proposed to enable its application to per-pixel computer vision tasks. Similarly, some other works [7, 28, 41] explored the role of data uncertainty by modeling both the mean and variance of the predictions. Uncertainty-based loss function of those works can be represented as:

$$\mathcal{L} = \frac{1}{N} \sum_{i=1}^N \frac{\|\mathbf{x}_i - f(\mathbf{y}_i)\|_2}{2\sigma_i^2} + \frac{1}{2} \ln \sigma_i^2 \quad (26)$$

where N denotes total number of input samples, \mathbf{x}_i is a target label, \mathbf{y}_i is an input, $f(\mathbf{y}_i)$ and σ_i^2 denote the learned mean and variance, respectively. Recent studies [35, 41] have continued to explore uncertainty estimation in deep learning, particularly in a task requiring high accuracy such as image super-resolution [35]. These approaches have demonstrated that such uncertainty-based losses that utilize uncertainty terms can achieve better results than mean square error (MSE) and mean absolute error (MAE) losses. Inspired by this work, we formulated our $\mathcal{L}_{\text{U-Diff}}$ as:

$$\mathcal{L}_{\text{U-Diff}} = \left\| \frac{1}{2\hat{\theta}} \odot \left| \hat{\mathbf{X}}_0 - \mathbf{X}_0 \right| + \frac{1}{2} \log \hat{\theta} \right\|_1, \quad (27)$$

where $\hat{\mathbf{X}}_0$ is a predicted residual, \mathbf{X}_0 is a target, and $\hat{\theta}$ serves as the estimated variance term and is regarded as the uncertainty map in our framework. In PAN-sharpening tasks, the regions with high uncertainty, such as complex textures and edges, are visually more significant than smooth areas. By prioritizing these regions, uncertainty-aware models can handle complex image details more effectively, potentially leading to improved PAN-sharpening performance in our U-Know-DiffPAN framework.

D. Additional Results

Table 8 presents the results of our proposed models, FSA-T and FSA-S, compared with all baseline models on the WV3, QB, and GF2 datasets. The evaluation includes Reduced-Resolution (RR), Full-Resolution (FR), and standard deviation. Fig. 10 to 15 illustrate the qualitative results for the WV3, QB, and GF2 datasets in both Reduced-Resolution and Full-Resolution settings. For the RR results, we visualize the RGB outputs, along with the difference between the output HRMS $\hat{\mathbf{I}}_{\text{MS}}^{\text{HR}}$ and the ground truth $\mathbf{I}_{\text{MS}}^{\text{HR}}$ using error maps and their corresponding mean absolute error (MAE) values. For the FR results, we showcase visual comparisons with the latest state-of-the-art methods. From the visual comparisons, we observe that our U-Know-DiffPAN framework significantly enhances restoration qualities, particularly in the regions with high-frequency contents, high uncertainty, and complex textures, such as edges and small objects. In RR scenarios, these regions exhibit a closer resemblance to their ground truths, compared to the previous

WV3		Reduced-Resolution						Full-Resolution		
Model	PSNR \uparrow	SSIM \uparrow	SAM \downarrow	ERGAS \downarrow	SCC \uparrow	Q8 \uparrow	D λ \downarrow	D s \downarrow	HQNR \uparrow	
PanNet[61]	36.148 \pm 1.958	0.966 \pm 0.011	3.402 \pm 0.672	2.538 \pm 0.597	0.979 \pm 0.006	0.913 \pm 0.087	0.035 \pm 0.014	0.049 \pm 0.019	0.918 \pm 0.031	
MSDCNN[64]	36.329 \pm 1.748	0.967 \pm 0.010	3.300 \pm 0.654	2.489 \pm 0.620	0.979 \pm 0.007	0.914 \pm 0.087	0.028 \pm 0.013	0.050 \pm 0.020	0.924 \pm 0.030	
FusionNet[56]	36.569 \pm 1.666	0.968 \pm 0.009	3.188 \pm 0.628	2.428 \pm 0.621	0.981 \pm 0.007	0.916 \pm 0.087	0.029 \pm 0.011	0.053 \pm 0.021	0.920 \pm 0.030	
LAGNet[26]	36.732 \pm 1.723	0.970 \pm 0.009	3.153 \pm 0.608	2.380 \pm 0.617	0.981 \pm 0.007	0.916 \pm 0.087	0.033 \pm 0.012	0.055 \pm 0.023	0.915 \pm 0.033	
S2DBPN[68]	37.216 \pm 1.888	0.972 \pm 0.009	3.019 \pm 0.588	2.245 \pm 0.541	0.985 \pm 0.005	0.917 \pm 0.091	0.025 \pm 0.010	0.030 \pm 0.010	0.946 \pm 0.018	
DCPNet[72]	37.009 \pm 1.735	0.972 \pm 0.008	3.083 \pm 0.537	2.301 \pm 0.569	0.984 \pm 0.005	0.915 \pm 0.092	0.043 \pm 0.018	0.036 \pm 0.012	0.923 \pm 0.027	
CANConv[15]	37.441 \pm 1.788	0.973 \pm 0.008	2.927 \pm 0.536	2.163 \pm 0.481	0.985 \pm 0.005	0.918 \pm 0.082	0.020 \pm 0.008	<u>0.030 \pm 0.008</u>	0.951 \pm 0.013	
PanDiff[33]	37.029 \pm 1.796	0.971 \pm 0.008	3.058 \pm 0.567	2.276 \pm 0.545	0.984 \pm 0.004	0.913 \pm 0.084	0.014 \pm 0.005	0.034 \pm 0.005	0.952 \pm 0.009	
TMDiff[59]	37.477 \pm 1.923	<u>0.973 \pm 0.008</u>	2.885 \pm 0.549	2.151 \pm 0.458	0.986 \pm 0.004	0.915 \pm 0.086	0.018 \pm 0.007	0.059 \pm 0.009	0.924 \pm 0.015	
FSA-T	<u>37.894 \pm 1.820</u>	0.976 \pm 0.007	<u>2.801 \pm 0.517</u>	<u>2.055 \pm 0.463</u>	0.987 \pm 0.003	<u>0.921 \pm 0.083</u>	0.014 \pm 0.005	0.032 \pm 0.003	<u>0.954 \pm 0.006</u>	
FSA-S	37.930 \pm 1.824	0.976 \pm 0.007	2.797 \pm 0.526	2.046 \pm 0.454	0.988 \pm 0.003	0.922 \pm 0.083	<u>0.016 \pm 0.006</u>	0.029 \pm 0.003	0.955 \pm 0.008	
QB		Reduced-Resolution						Full-Resolution		
Model	PSNR \uparrow	SSIM \uparrow	SAM \downarrow	ERGAS \downarrow	SCC \uparrow	Q4 \uparrow	D λ \downarrow	D s \downarrow	HQNR \uparrow	
PanNet[61]	35.563 \pm 1.930	0.939 \pm 0.012	5.273 \pm 0.946	4.856 \pm 0.590	0.966 \pm 0.015	0.911 \pm 0.094	0.063 \pm 0.019	0.092 \pm 0.021	0.851 \pm 0.035	
MSDCNN[64]	37.040 \pm 1.778	0.954 \pm 0.007	4.828 \pm 0.824	4.074 \pm 0.244	0.977 \pm 0.010	0.925 \pm 0.098	0.058 \pm 0.014	0.058 \pm 0.027	0.888 \pm 0.037	
FusionNet[56]	36.821 \pm 1.765	0.952 \pm 0.007	4.892 \pm 0.822	4.183 \pm 0.266	0.975 \pm 0.011	0.923 \pm 0.100	0.074 \pm 0.022	0.079 \pm 0.025	0.853 \pm 0.041	
LAGNet[26]	37.565 \pm 1.721	0.958 \pm 0.006	4.682 \pm 0.785	3.845 \pm 0.323	0.980 \pm 0.009	0.930 \pm 0.095	0.075 \pm 0.019	0.035 \pm 0.009	0.892 \pm 0.024	
S2DBPN[68]	37.314 \pm 1.782	0.956 \pm 0.006	4.849 \pm 0.822	3.956 \pm 0.291	0.980 \pm 0.008	0.928 \pm 0.093	0.059 \pm 0.026	0.036 \pm 0.023	0.908 \pm 0.044	
DCPNet[72]	38.079 \pm 1.454	<u>0.963 \pm 0.004</u>	4.420 \pm 0.710	3.618 \pm 0.313	0.983 \pm 0.010	0.935 \pm 0.095	0.051 \pm 0.017	0.073 \pm 0.013	0.880 \pm 0.013	
CANConv[15]	37.795 \pm 1.801	0.960 \pm 0.006	4.554 \pm 0.788	3.740 \pm 0.304	0.982 \pm 0.007	0.935 \pm 0.087	0.039 \pm 0.012	0.070 \pm 0.017	0.893 \pm 0.010	
PanDiff[33]	37.842 \pm 1.721	0.959 \pm 0.006	4.611 \pm 0.768	3.723 \pm 0.280	0.982 \pm 0.007	0.935 \pm 0.084	0.028 \pm 0.011	0.055 \pm 0.012	0.919 \pm 0.010	
TMDiff[59]	37.642 \pm 1.831	0.958 \pm 0.006	4.627 \pm 0.814	3.804 \pm 0.279	0.981 \pm 0.008	0.930 \pm 0.096	<u>0.034 \pm 0.016</u>	0.068 \pm 0.012	0.901 \pm 0.011	
FSA-T	<u>38.343 \pm 1.718</u>	0.964 \pm 0.005	<u>4.349 \pm 0.723</u>	<u>3.502 \pm 0.272</u>	0.985 \pm 0.007	0.938 \pm 0.089	0.036 \pm 0.018	0.031 \pm 0.014	0.934 \pm 0.029	
FSA-S	38.361 \pm 1.709	0.964 \pm 0.005	4.337 \pm 0.733	3.500 \pm 0.272	0.984 \pm 0.007	0.938 \pm 0.090	0.035 \pm 0.011	<u>0.035 \pm 0.021</u>	<u>0.931 \pm 0.029</u>	
GF2		Reduced-Resolution						Full-Resolution		
Model	PSNR \uparrow	SSIM \uparrow	SAM \downarrow	ERGAS \downarrow	SCC \uparrow	Q4 \uparrow	D λ \downarrow	D s \downarrow	HQNR \uparrow	
PanNet[61]	39.197 \pm 2.009	0.959 \pm 0.011	1.050 \pm 0.209	1.038 \pm 0.214	0.975 \pm 0.006	0.963 \pm 0.009	0.020 \pm 0.012	0.052 \pm 0.009	0.929 \pm 0.013	
MSDCNN[64]	40.730 \pm 1.564	0.971 \pm 0.006	0.946 \pm 0.166	0.862 \pm 0.141	0.983 \pm 0.003	0.972 \pm 0.009	0.026 \pm 0.014	0.079 \pm 0.011	0.898 \pm 0.016	
FusionNet[56]	39.866 \pm 1.955	0.966 \pm 0.009	0.971 \pm 0.195	0.960 \pm 0.193	0.980 \pm 0.005	0.967 \pm 0.008	0.034 \pm 0.013	0.105 \pm 0.013	0.865 \pm 0.018	
LAGNet[26]	41.147 \pm 1.384	0.974 \pm 0.005	0.886 \pm 0.140	0.816 \pm 0.121	0.985 \pm 0.003	0.974 \pm 0.009	0.030 \pm 0.014	0.078 \pm 0.013	0.895 \pm 0.021	
S2DBPN[68]	42.686 \pm 1.676	0.980 \pm 0.005	0.772 \pm 0.149	0.686 \pm 0.125	0.990 \pm 0.002	0.981 \pm 0.007	0.020 \pm 0.012	0.046 \pm 0.007	0.935 \pm 0.011	
DCPNet[72]	42.312 \pm 1.682	0.979 \pm 0.005	0.806 \pm 0.153	0.724 \pm 0.138	0.988 \pm 0.003	0.980 \pm 0.007	0.024 \pm 0.022	0.024 \pm 0.008	0.953 \pm 0.019	
CANConv[15]	43.166 \pm 1.705	0.982 \pm 0.004	0.722 \pm 0.138	0.653 \pm 0.124	0.991 \pm 0.002	0.983 \pm 0.006	0.019 \pm 0.010	0.063 \pm 0.009	0.919 \pm 0.011	
PanDiff[33]	42.827 \pm 1.462	0.980 \pm 0.005	0.767 \pm 0.134	0.674 \pm 0.110	0.990 \pm 0.002	0.981 \pm 0.007	0.020 \pm 0.014	0.045 \pm 0.009	0.936 \pm 0.011	
TMDiff[59]	41.896 \pm 1.765	0.977 \pm 0.005	0.764 \pm 0.155	0.754 \pm 0.143	0.988 \pm 0.003	0.979 \pm 0.007	0.029 \pm 0.011	<u>0.030 \pm 0.010</u>	0.942 \pm 0.016	
FSA-T	44.757 \pm 1.359	0.988 \pm 0.003	0.603 \pm 0.102	0.537 \pm 0.077	0.994 \pm 0.001	0.988 \pm 0.006	0.017 \pm 0.010	<u>0.030 \pm 0.008</u>	0.953 \pm 0.013	
FSA-S	<u>44.585 \pm 1.521</u>	<u>0.986 \pm 0.003</u>	<u>0.624 \pm 0.109</u>	<u>0.548 \pm 0.091</u>	<u>0.993 \pm 0.001</u>	<u>0.987 \pm 0.007</u>	<u>0.018 \pm 0.011</u>	0.037 \pm 0.007	<u>0.944 \pm 0.012</u>	

Table 8. Additional PAN-sharpening results by our U-Know-DiffPAN and other SOTA methods for the WV3, QB, and GF2 dataset. The best (second best) performance in each block is highlighted in bold red (underlined in blue).

methods. Even in FR scenarios where ground truth is unavailable, our U-Know-DiffPAN framework produces more detailed and robust results, demonstrating superior structural and spectral fidelity in high-uncertainty regions. This highlights the capability of our U-Know-DiffPAN to outperform state-of-the-art models in both qualitative and quantitative aspects.

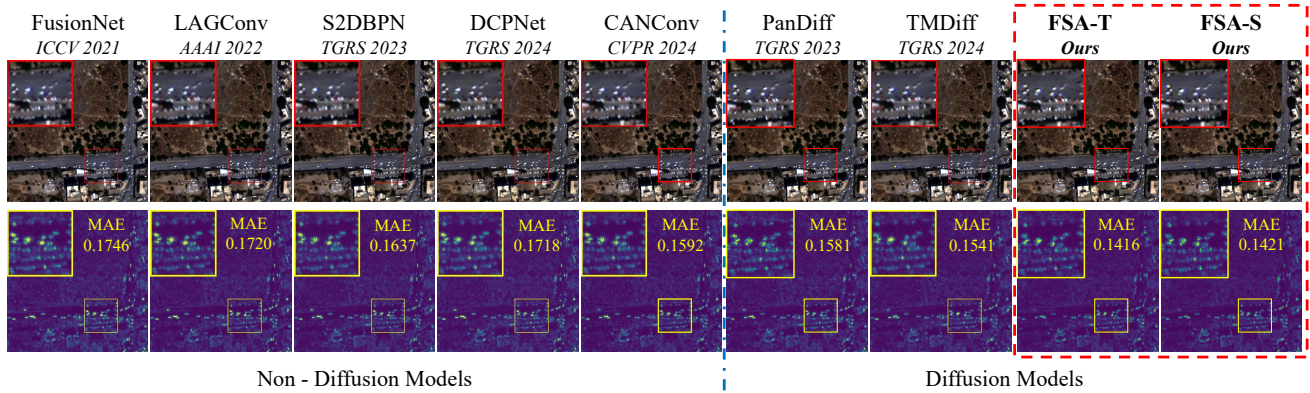


Figure 10. PAN-sharpening results for the WV3 dataset under reduced resolution (RR) scenarios. The first row depicts the output HRMS images, while the second row highlights the Error Map between the output HRMS and the corresponding ground truth images. The Mean Absolute Error (MAE) values are presented alongside the Error Map. Zoom in for better visualization.

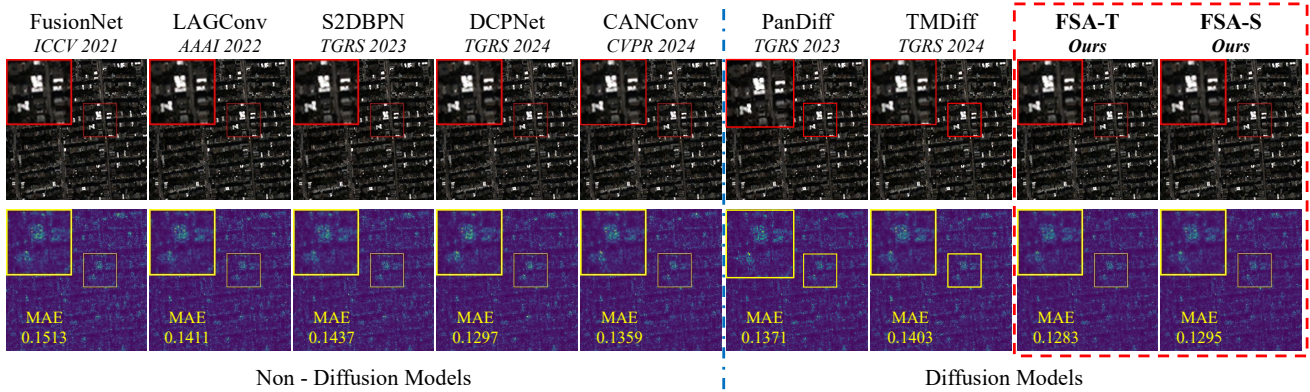


Figure 11. PAN-sharpening results for the QB dataset under reduced resolution (RR) scenarios. The first row depicts the output HRMS images, while the second row highlights the Error Map between the output HRMS and the corresponding ground truth images. The Mean Absolute Error (MAE) values are presented alongside the Error Map. Zoom in for better visualization.

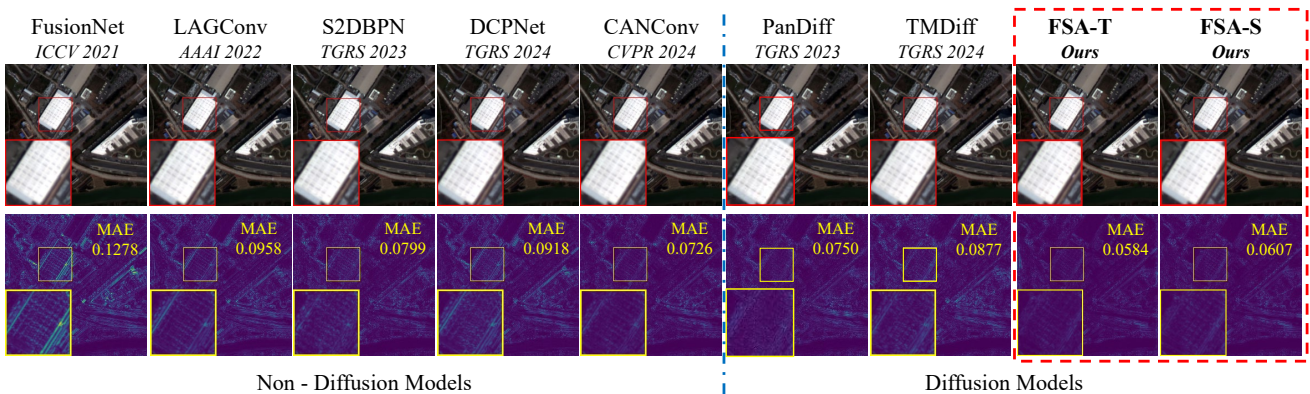


Figure 12. PAN-sharpening results for the GF2 dataset under reduced resolution (RR) scenarios. The first row depicts the output HRMS images, while the second row highlights the Error Map between the output HRMS and the corresponding ground truth images. The Mean Absolute Error (MAE) values are presented alongside the Error Map. Zoom in for better visualization.

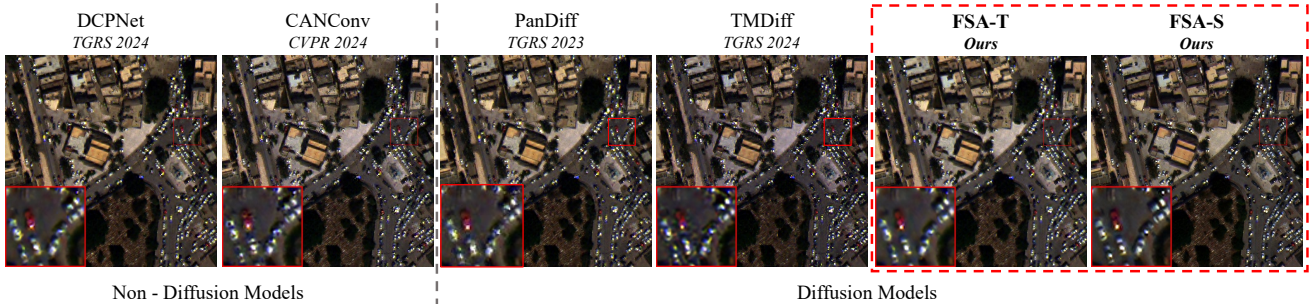


Figure 13. PAN-sharpening results for the WV3 dataset under full resolution (FR) scenarios. The first row depicts the output HRMS images. Zoom in for better visualization.

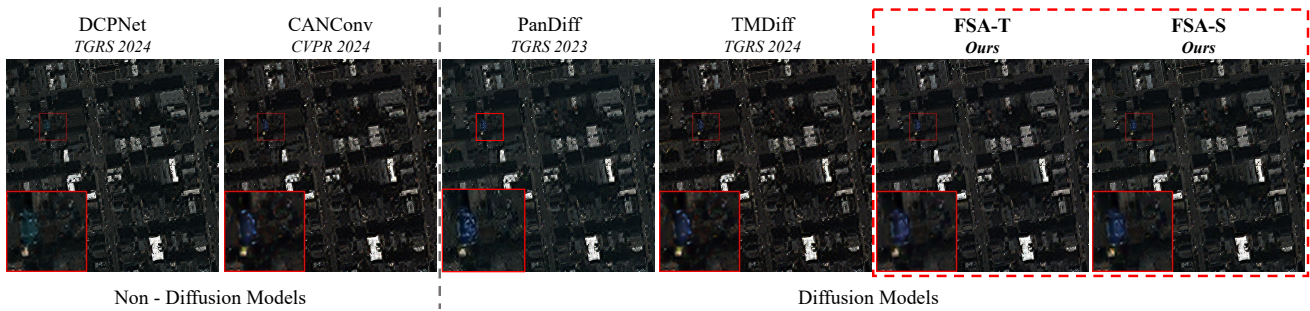


Figure 14. PAN-sharpening results for the QB dataset under full resolution (FR) scenarios. The first row depicts the output HRMS images. Zoom in for better visualization.

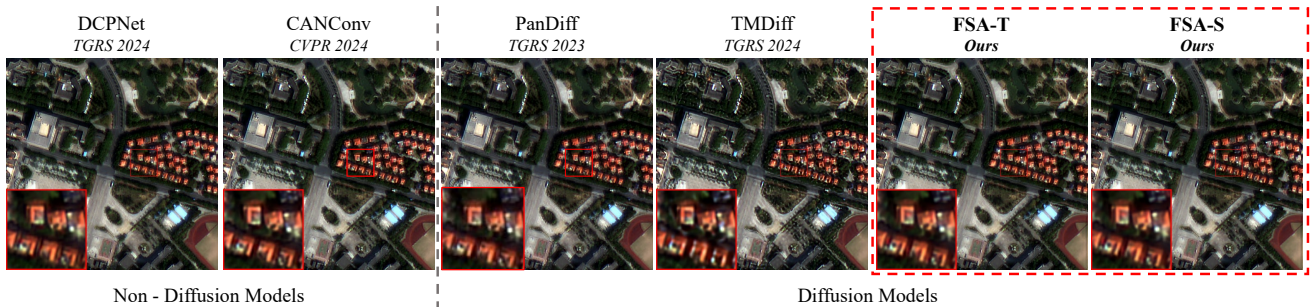


Figure 15. PAN-sharpening results for the GF2 dataset under full resolution (FR) scenarios. The first row depicts the output HRMS images. Zoom in for better visualization.

References

- [1] Bruno Aiuzzi, Luciano Alparone, Stefano Baronti, Andrea Garzelli, and Massimo Selva. Mtf-tailored multiscale fusion of high-resolution ms and pan imagery. *Photogrammetric Engineering & Remote Sensing*, 72(5):591–596, 2006. 2, 10
- [2] Israa Amro, Javier Mateos, Miguel Vega, Rafael Molina, and Aggelos K Katsaggelos. A survey of classical methods and new trends in pansharpening of multispectral images. *EURASIP Journal on Advances in Signal Processing*, 2011:1–22, 2011. 1
- [3] Arsenii Ashukha, Alexander Lyzhov, Dmitry Molchanov, and Dmitry Vetrov. Pitfalls of in-domain uncertainty estimation and ensembling in deep learning. *arXiv preprint arXiv:2002.06470*, 2020. 11
- [4] Coloma Ballester, Vicent Caselles, Laura Igual, Joan Verdera, and Bernard Rougé. A variational model for p+xs image fusion. *International Journal of Computer Vision*, 69:43–58, 2006. 2
- [5] Jonathan T Barron. A general and adaptive robust loss function. In *Proceedings of the IEEE/CVF conference on computer vision and pattern recognition*, pages 4331–4339, 2019. 6
- [6] Enrico Celeghini, Manuel Gadella, and Mariano A del Olmo. Hermite functions and fourier series. *Symmetry*, 13(5):853, 2021. 5
- [7] Jie Chang, Zhonghao Lan, Changmao Cheng, and Yichen Wei. Data uncertainty learning in face recognition. In *Proceedings of the IEEE/CVF conference on computer vision and pattern recognition*, pages 5710–5719, 2020. 11
- [8] Wei-Chun Chen, Chia-Che Chang, and Che-Rung Lee. Knowledge distillation with feature maps for image classification. In *Computer Vision–ACCV 2018: 14th Asian Conference on Computer Vision, Perth, Australia, December 2–6, 2018, Revised Selected Papers, Part III 14*, pages 200–215. Springer, 2019. 3
- [9] Jaewan Choi, Kiyun Yu, and Yongil Kim. A new adaptive component-substitution-based satellite image fusion by using partial replacement. *IEEE transactions on geoscience and remote sensing*, 49(1):295–309, 2010. 2
- [10] Matteo Ciotola, Sergio Vitale, Antonio Mazza, Giovanni Poggi, and Giuseppe Scarpa. Pansharpening by convolutional neural networks in the full resolution framework. *IEEE Transactions on Geoscience and Remote Sensing*, 60:1–17, 2022. 2
- [11] Matteo Ciotola, Giuseppe Guarino, Gemine Vivone, Giovanni Poggi, Jocelyn Chanussot, Antonio Plaza, and Giuseppe Scarpa. Hyperspectral pansharpening: Critical review, tools and future perspectives. *arXiv preprint arXiv:2407.01355*, 2024. 1
- [12] Liang-Jian Deng, Gemine Vivone, Mercedes E Paoletti, Giuseppe Scarpa, Jiang He, Yongjun Zhang, Jocelyn Chanussot, and Antonio Plaza. Machine learning in pansharpening: A benchmark, from shallow to deep networks. *IEEE Geoscience and Remote Sensing Magazine*, 10(3):279–315, 2022. 2, 6
- [13] P Kingma Diederik. Adam: A method for stochastic optimization. (*No Title*), 2014. 6
- [14] Kento Doi and Akira Iwasaki. Sscnet: Spectral-spatial consistency optimization of cnn for pansharpening. In *IGARSS 2019-2019 IEEE International Geoscience and Remote Sensing Symposium*, pages 3141–3144. IEEE, 2019. 2
- [15] Yule Duan, Xiao Wu, Haoyu Deng, and Liang-Jian Deng. Content-adaptive non-local convolution for remote sensing pansharpening. In *Proceedings of the IEEE/CVF Conference on Computer Vision and Pattern Recognition*, pages 27738–27747, 2024. 1, 2, 7, 12
- [16] Joan Duran, Antoni Buades, Bartomeu Coll, Catalina Sbert, and Gwendoline Blanchet. A survey of pansharpening methods with a new band-decoupled variational model. *ISPRS Journal of Photogrammetry and Remote Sensing*, 125:78–105, 2017. 1
- [17] Andrea Garzelli and Filippo Nencini. Hypercomplex quality assessment of multi/hyperspectral images. *IEEE Geoscience and Remote Sensing Letters*, 6(4):662–665, 2009. 6
- [18] Anaïs Gastineau, Jean-François Aujol, Yannick Berthoumieu, and Christian Germain. A residual dense generative adversarial network for pansharpening with geometrical constraints. In *2020 IEEE International Conference on Image Processing (ICIP)*, pages 493–497. IEEE, 2020. 2
- [19] Ian Goodfellow, Jean Pouget-Abadie, Mehdi Mirza, Bing Xu, David Warde-Farley, Sherjil Ozair, Aaron Courville, and Yoshua Bengio. Generative adversarial nets. *Advances in neural information processing systems*, 27, 2014. 2
- [20] Dan Hendrycks and Kevin Gimpel. Gaussian error linear units (gelus). *arXiv preprint arXiv:1606.08415*, 2016. 5
- [21] Geoffrey Hinton. Distilling the knowledge in a neural network. *arXiv preprint arXiv:1503.02531*, 2015. 3
- [22] Jonathan Ho, Ajay Jain, and Pieter Abbeel. Denoising diffusion probabilistic models. *Advances in neural information processing systems*, 33:6840–6851, 2020. 2, 3
- [23] Jianwen Hu, Pei Hu, Xudong Kang, Hui Zhang, and Shaosheng Fan. Pan-sharpening via multiscale dynamic convolutional neural network. *IEEE Transactions on Geoscience and Remote Sensing*, 59(3):2231–2244, 2020. 2
- [24] Wei Huang, Liang Xiao, Zhihui Wei, Hongyi Liu, and Songze Tang. A new pan-sharpening method with deep neural networks. *IEEE Geoscience and Remote Sensing Letters*, 12(5):1037–1041, 2015. 2
- [25] Zeyi Huang, Yang Zou, BVK Kumar, and Dong Huang. Comprehensive attention self-distillation for weakly-supervised object detection. *Advances in neural information processing systems*, 33:16797–16807, 2020. 3
- [26] Zi-Rong Jin, Tian-Jing Zhang, Tai-Xiang Jiang, Gemine Vivone, and Liang-Jian Deng. Lagconv: Local-context adaptive convolution kernels with global harmonic bias for pansharpening. In *Proceedings of the AAAI Conference on Artificial Intelligence*, pages 1113–1121, 2022. 2, 7, 12
- [27] Tero Karras, Samuli Laine, and Timo Aila. A style-based generator architecture for generative adversarial networks. In *Proceedings of the IEEE/CVF conference on computer vision and pattern recognition*, pages 4401–4410, 2019. 2, 4
- [28] Alex Kendall and Yarin Gal. What uncertainties do we need in bayesian deep learning for computer vision? *Advances in neural information processing systems*, 30, 2017. 11

- [29] Balaji Lakshminarayanan, Alexander Pritzel, and Charles Blundell. Simple and scalable predictive uncertainty estimation using deep ensembles. *Advances in neural information processing systems*, 30, 2017. 11
- [30] Xiaobo Liu, Xiang Liu, Haoran Dai, Xudong Kang, Antonio Plaza, and Wenjie Zu. Mun-gan: A multiscale unsupervised network for remote sensing image pansharpening. *IEEE Transactions on Geoscience and Remote Sensing*, 61: 1–18, 2023. 2
- [31] Laetitia Loncan, Luis B De Almeida, José M Bioucas-Dias, Xavier Briottet, Jocelyn Chanussot, Nicolas Dobigeon, Sophie Fabre, Wenzhi Liao, Giorgio A Licciardi, Miguel Simoes, et al. Hyperspectral pansharpening: A review. *IEEE Geoscience and remote sensing magazine*, 3(3):27–46, 2015. 1
- [32] Jiayi Ma, Wei Yu, Chen Chen, Pengwei Liang, Xiaojie Guo, and Junjun Jiang. Pan-gan: An unsupervised pan-sharpening method for remote sensing image fusion. *Information Fusion*, 62:110–120, 2020. 2
- [33] Qingyan Meng, Wenxu Shi, Sijia Li, and Linlin Zhang. Pan-diff: A novel pansharpening method based on denoising diffusion probabilistic model. *IEEE Transactions on Geoscience and Remote Sensing*, 61:1–17, 2023. 1, 2, 6, 7, 8, 12
- [34] Guy P Nason and Bernard W Silverman. The stationary wavelet transform and some statistical applications. In *Wavelets and statistics*, pages 281–299. Springer, 1995. 3, 4, 5
- [35] Qian Ning, Weisheng Dong, Xin Li, Jinjian Wu, and Guangming Shi. Uncertainty-driven loss for single image super-resolution. *Advances in Neural Information Processing Systems*, 34:16398–16409, 2021. 4, 11
- [36] Xavier Otazu, María González-Audiciana, Octavi Fors, and Jorge Núñez. Introduction of sensor spectral response into image fusion methods. application to wavelet-based methods. *IEEE Transactions on Geoscience and Remote Sensing*, 43(10):2376–2385, 2005. 2, 10
- [37] Hao Phung, Quan Dao, and Anh Tran. Wavelet diffusion models are fast and scalable image generators. In *Proceedings of the IEEE/CVF conference on computer vision and pattern recognition*, pages 10199–10208, 2023. 5, 9
- [38] Alec Radford, Jong Wook Kim, Chris Hallacy, Aditya Ramesh, Gabriel Goh, Sandhini Agarwal, Girish Sastry, Amanda Askell, Pamela Mishkin, Jack Clark, et al. Learning transferable visual models from natural language supervision. In *International conference on machine learning*, pages 8748–8763. PMLR, 2021. 3
- [39] Olaf Ronneberger, Philipp Fischer, and Thomas Brox. U-net: Convolutional networks for biomedical image segmentation. In *Medical image computing and computer-assisted intervention—MICCAI 2015: 18th international conference, Munich, Germany, October 5–9, 2015, proceedings, part III 18*, pages 234–241. Springer, 2015. 4
- [40] Chitwan Saharia, Jonathan Ho, William Chan, Tim Salimans, David J Fleet, and Mohammad Norouzi. Image super-resolution via iterative refinement. *IEEE transactions on pattern analysis and machine intelligence*, 45(4):4713–4726, 2022. 2
- [41] Maximilian Seitzer, Arash Tavakoli, Dimitrije Antic, and Georg Martius. On the pitfalls of heteroscedastic uncertainty estimation with probabilistic neural networks. *arXiv preprint arXiv:2203.09168*, 2022. 4, 11
- [42] Shuyao Shang, Zhengyang Shan, Guangxing Liu, LunQian Wang, XingHua Wang, Zekai Zhang, and Jinglin Zhang. Resdiff: Combining cnn and diffusion model for image super-resolution. In *Proceedings of the AAAI Conference on Artificial Intelligence*, pages 8975–8983, 2024. 5, 9
- [43] Mark J Shensa et al. The discrete wavelet transform: wedding the a trous and mallat algorithms. *IEEE Transactions on signal processing*, 40(10):2464–2482, 1992. 2
- [44] Jiaming Song, Chenlin Meng, and Stefano Ermon. Denoising diffusion implicit models. *arXiv preprint arXiv:2010.02502*, 2020. 2, 6
- [45] Baoli Sun, Xinchun Ye, Baopu Li, Haojie Li, Zhihui Wang, and Rui Xu. Learning scene structure guidance via cross-task knowledge transfer for single depth super-resolution. In *Proceedings of the IEEE/CVF conference on computer vision and pattern recognition*, pages 7792–7801, 2021. 3
- [46] Joost Van Amersfoort, Lewis Smith, Yee Whye Teh, and Yarin Gal. Uncertainty estimation using a single deep deterministic neural network. In *International conference on machine learning*, pages 9690–9700. PMLR, 2020. 11
- [47] Gemine Vivone, Luciano Alparone, Jocelyn Chanussot, Mauro Dalla Mura, Andrea Garzelli, Giorgio A Licciardi, Rocco Restaino, and Lucien Wald. A critical comparison among pansharpening algorithms. *IEEE Transactions on Geoscience and Remote Sensing*, 53(5):2565–2586, 2014. 6
- [48] Gemine Vivone, Mauro Dalla Mura, Andrea Garzelli, Rocco Restaino, Giuseppe Scarpa, Magnus O Ulfarsson, Luciano Alparone, and Jocelyn Chanussot. A new benchmark based on recent advances in multispectral pansharpening: Revisiting pansharpening with classical and emerging pansharpening methods. *IEEE Geoscience and Remote Sensing Magazine*, 9(1):53–81, 2020. 6
- [49] Lucien Wald. Quality of high resolution synthesised images: Is there a simple criterion? In *Third conference " Fusion of Earth data: merging point measurements, raster maps and remotely sensed images "*, pages 99–103. SEE/URISCA, 2000. 6
- [50] Lucien Wald, Thierry Ranchin, and Marc Mangolini. Fusion of satellite images of different spatial resolutions: Assessing the quality of resulting images. *Photogrammetric engineering and remote sensing*, 63(6):691–699, 1997. 2
- [51] Jianyi Wang, Zongsheng Yue, Shangchen Zhou, Kelvin CK Chan, and Chen Change Loy. Exploiting diffusion prior for real-world image super-resolution. *International Journal of Computer Vision*, pages 1–21, 2024. 2
- [52] Tao Wang, Li Yuan, Xiaopeng Zhang, and Jiashi Feng. Distilling object detectors with fine-grained feature imitation. In *Proceedings of the IEEE/CVF Conference on Computer Vision and Pattern Recognition*, pages 4933–4942, 2019. 3
- [53] Xintao Wang, Ke Yu, Chao Dong, and Chen Change Loy. Recovering realistic texture in image super-resolution by deep spatial feature transform. In *Proceedings of the IEEE conference on computer vision and pattern recognition*, pages 606–615, 2018. 4

- [54] Zhou Wang, Alan C Bovik, Hamid R Sheikh, and Eero P Simoncelli. Image quality assessment: from error visibility to structural similarity. *IEEE transactions on image processing*, 13(4):600–612, 2004. [6](#)
- [55] Stephen Weinstein and Paul Ebert. Data transmission by frequency-division multiplexing using the discrete fourier transform. *IEEE transactions on Communication Technology*, 19(5):628–634, 1971. [2](#)
- [56] Xiao Wu, Ting-Zhu Huang, Liang-Jian Deng, and Tian-Jing Zhang. Dynamic cross feature fusion for remote sensing pansharpening. In *Proceedings of the IEEE/CVF International Conference on Computer Vision*, pages 14687–14696, 2021. [7](#), [12](#)
- [57] Yuxin Wu and Kaiming He. Group normalization. In *Proceedings of the European conference on computer vision (ECCV)*, pages 3–19, 2018. [5](#)
- [58] Bin Xia, Yulun Zhang, Shiyin Wang, Yitong Wang, Xinglong Wu, Yapeng Tian, Wenming Yang, and Luc Van Gool. Diffir: Efficient diffusion model for image restoration. In *Proceedings of the IEEE/CVF International Conference on Computer Vision*, pages 13095–13105, 2023. [2](#), [4](#)
- [59] Yinghui Xing, Litao Qu, Shizhou Zhang, Jiapeng Feng, Xiuwei Zhang, and Yanning Zhang. Empower generalizability for pansharpening through text-modulated diffusion model. *IEEE Transactions on Geoscience and Remote Sensing*, 2024. [1](#), [2](#), [3](#), [6](#), [7](#), [8](#), [12](#)
- [60] Kunran Xu, Lai Rui, Yishi Li, and Lin Gu. Feature normalized knowledge distillation for image classification. In *European conference on computer vision*, pages 664–680. Springer, 2020. [3](#)
- [61] Junfeng Yang, Xueyang Fu, Yuwen Hu, Yue Huang, Xinghao Ding, and John Paisley. Pannet: A deep network architecture for pan-sharpening. In *Proceedings of the IEEE international conference on computer vision*, pages 5449–5457, 2017. [2](#), [7](#), [12](#)
- [62] Zhendong Yang, Zhe Li, Ailing Zeng, Zexian Li, Chun Yuan, and Yu Li. Vitkd: Feature-based knowledge distillation for vision transformers. In *Proceedings of the IEEE/CVF Conference on Computer Vision and Pattern Recognition*, pages 1379–1388, 2024. [3](#)
- [63] Lewei Yao, Renjie Pi, Hang Xu, Wei Zhang, Zhenguo Li, and Tong Zhang. G-detkd: Towards general distillation framework for object detectors via contrastive and semantic-guided feature imitation. In *Proceedings of the IEEE/CVF international conference on computer vision*, pages 3591–3600, 2021. [3](#)
- [64] Qiangqiang Yuan, Yancong Wei, Xiangchao Meng, Huanfeng Shen, and Liangpei Zhang. A multiscale and multidepth convolutional neural network for remote sensing imagery pansharpening. *IEEE Journal of Selected Topics in Applied Earth Observations and Remote Sensing*, 11(3):978–989, 2018. [7](#), [12](#)
- [65] Roberta H Yuhas, Alexander FH Goetz, and Joe W Boardman. Discrimination among semi-arid landscape endmembers using the spectral angle mapper (sam) algorithm. In *JPL, Summaries of the Third Annual JPL Airborne Geoscience Workshop. Volume 1: AVIRIS Workshop*, 1992. [6](#)
- [66] Syed Waqas Zamir, Aditya Arora, Salman Khan, Munawar Hayat, Fahad Shahbaz Khan, and Ming-Hsuan Yang. Restormer: Efficient transformer for high-resolution image restoration. In *Proceedings of the IEEE/CVF conference on computer vision and pattern recognition*, pages 5728–5739, 2022. [5](#)
- [67] Jie Zhang, Xuanhua He, Keyu Yan, Ke Cao, Rui Li, Chengjun Xie, Man Zhou, and Danfeng Hong. Pansharpening with wavelet-enhanced high-frequency information. *IEEE Transactions on Geoscience and Remote Sensing*, 62:1–14, 2024. [9](#)
- [68] Kai Zhang, Anfei Wang, Feng Zhang, Wenbo Wan, Jiande Sun, and Lorenzo Bruzzone. Spatial-spectral dual back-projection network for pansharpening. *IEEE Transactions on Geoscience and Remote Sensing*, 2023. [2](#), [7](#), [12](#)
- [69] Yiman Zhang, Hanting Chen, Xinghao Chen, Yiping Deng, Chunjing Xu, and Yunhe Wang. Data-free knowledge distillation for image super-resolution. In *Proceedings of the IEEE/CVF Conference on Computer Vision and Pattern Recognition*, pages 7852–7861, 2021. [3](#)
- [70] Yun Zhang, Wei Li, Simiao Li, Hanting Chen, Zhijun Tu, Wenjia Wang, Bingyi Jing, Shaohui Lin, and Jie Hu. Data upcycling knowledge distillation for image super-resolution. *arXiv preprint arXiv:2309.14162*, 2023. [3](#)
- [71] Yaqun Zhang, Zhichang Guo, Dazhi Zhang, and Boying Wu. An anisotropic variational pansharpening model with adaptive coefficients. *Inverse Problems and Imaging*, pages 0–0, 2024. [1](#)
- [72] Yafei Zhang, Xuji Yang, Huafeng Li, Minghong Xie, and Zhengtao Yu. Depnet: A dual-task collaborative promotion network for pansharpening. *IEEE Transactions on Geoscience and Remote Sensing*, 62:1–16, 2024. [2](#), [7](#), [12](#)
- [73] Hao Zheng, Zhanlei Yang, Wenju Liu, Jizhong Liang, and Yanpeng Li. Improving deep neural networks using softplus units. In *2015 International joint conference on neural networks (IJCNN)*, pages 1–4. IEEE, 2015. [4](#)
- [74] Wu Zheng, Weiliang Tang, Li Jiang, and Chi-Wing Fu. Sessd: Self-ensembling single-stage object detector from point cloud. In *Proceedings of the IEEE/CVF conference on computer vision and pattern recognition*, pages 14494–14503, 2021. [3](#)
- [75] Jie Zhou, Daniel L Civco, and John A Silander. A wavelet transform method to merge landsat tm and spot panchromatic data. *International journal of remote sensing*, 19(4):743–757, 1998. [5](#), [10](#)